

Metachronal waves in concentrations of swimming *Turbatrix aceti* nematodes and an oscillator chain model for their coordinated motions

A. C. Quillen,^{1,*} A. Peshkov,^{1,†} Esteban Wright,^{1,‡} and Sonia McGaffigan^{1,§}

¹*Department of Physics and Astronomy, University of Rochester, Rochester, NY 14627, USA*

At high concentration, free swimming nematodes known as vinegar eels (*Turbatrix aceti*), collectively exhibit metachronal waves near a boundary. We find that the frequency of the collective traveling wave is lower than that of the freely swimming organisms. We explore models based on a chain of oscillators with nearest neighbor interactions that inhibit oscillator phase velocity. The phase of each oscillator represents the phase of the motion of the eel's head back and forth about its mean position. A strongly interacting directed chain model mimicking steric repulsion between organisms robustly gives traveling wave states and can approximately match the observed wavelength and oscillation frequency of the observed traveling wave. We predict body shapes assuming that waves propagate down the eel body at a constant speed. The phase oscillator model that impedes eel head overlaps also reduces close interactions throughout the eel bodies.

I. INTRODUCTION

Concentrations of biological organisms can be considered active materials as they are comprised of self-driven units and energy is continuously expended through locomotion [1]. Collective behavior of groups of organisms include flocking or swimming in schools [2, 3] and synchronization [4, 5]. Synchronization processes in nature include glowing rhythms of colonies of fireflies [4], crowd synchrony of pedestrians walking on a bridge [6] and flagella beating in phase with one another [7].

The head or tail of an individual snake, flagellum, cilium or nematode moves back and forth with respect to a mean position. This periodic motion can be described with a phase of oscillation (e.g., [8]). In concentrations of mobile oscillators, both synchronization and swarming can occur together, and such systems can display a rich diversity of collective states (e.g., the *swarmalators* studied by O’Keefe et al. [9]) including collectively organized and coordinated motions known as traveling or metachronal waves. A metachronal rhythm or metachronal wave refers to a locally synchronized motion of individuals with a delay between them, in contrast to globally synchronized patterns of oscillation.

Metachronal waves require coordinated motions between neighboring structures or organisms [10, 11]. Swimming spermatozoa synchronize the beating of their cilia, and flagellates can synchronize the motions of their flagella when they are in close proximity [7, 12–16]. When a constant phase difference or time delay is maintained between neighboring oscillating structures, the collective motion has the appearance of a traveling wave.

One approach to modeling metachronal wave formation in cilia or flagella is to model them as an array of flexible filaments that oscillate or beat when alone. Self-

organized metachronal waves then arise due to hydrodynamic [8, 11, 13, 14, 17–20] or steric [21] interactions between neighboring filaments. Even though a filament can bend and flex, its behavior can approximately be described with an angle or phase which specifies the position of its moving tip (e.g., [11, 13, 14]). Although each filament moves in three dimensions, simplified models consisting of discrete linear chains of interacting oscillators can describe the collective behavior [11, 13, 14].

Phase oscillator chain models, known as local Kuramoto models, exhibit both long lived synchronous and traveling wave states [22–27]. However, in many of these models, a system with randomly chosen initial phases is more likely to evolve into a synchronous state than a traveling wave state [26, 27]. Simple criteria are not available for predicting whether an interacting phase oscillator model is likely to give traveling wave states if initialized with random phases. However, physically motivated interacting phase oscillator models for metachronal waves in cilia and flagella have succeeded in robustly giving traveling wave states [13, 14].

In this study we report on collective behavior in a system of undulating free-swimming organisms, vinegar eels, species *Turbatrix aceti* (*T. aceti*), which are a type of free-living nematode. They are found living in beer mats, slime from tree wounds and cultures of edible vinegars. Because they are hardy, they are used in aquaculture by fish keepers and aquarists as food for newly hatched fish or crustaceans. Vinegar eels are tolerant of variation in acidity and they subsist on yeast. The metachronal waves in *T. aceti*, reported by Peshkov [28], Peshkov et al. [29], are similar to those seen in cilia. However, unlike cilia which are affixed to a cell membrane, the vinegar eels are freely swimming organisms. At about 1 mm in length, the vinegar eels are visible by naked eye and are much larger than cilia (typically a few μm in length) or flagella on colonies of microorganisms that display metachronal waves (e.g., with flagella length $\sim 10\mu\text{m}$; [14]). Concentrated suspensions of vinegar eels are a novel biological system in which we can study ensemble coordination and synchronization. Henceforth we refer to the vinegar eels

* alice.quillen@rochester.edu

† apeshkov@ur.rochester.edu

‡ ewrig15@ur.rochester.edu

§ smcgaffi@u.rochester.edu

colloquially as ‘eels’ even though they are nematodes.

Ensembles of active particles can exhibit a phase transition from gaseous to collective behavior at higher number density due to particle interactions (e.g., for unipolar self-propelled particles [30]). Metachronal waves are only present in high concentrations of vinegar eels [29] so interactions between them are necessary for the coordinated wave motion. Collective coordinated motion is likely to be mediated by the interactions between the organisms. In our study we compare the motion of the vinegar eels participating in metachronal waves to those that are freely swimming to probe the nature of these interactions.

While the well studied nematode *Caenorhabditis elegans* (*C. elegans*) naturally grows in soil, *C. elegans* is also an undulatory swimmer in water (e.g., [31]). *C. elegans* nematodes congregate near surfaces and boundaries (they exhibit bordertaxis) [31]. In close proximity, a pair of swimming *C. elegans* nematodes will synchronize their gait [32]. Collective behavior of *C. elegans* includes the formation of a network on a surface [33] and synchronization of clusters of tens of nematodes [32]. We have observed similarities between the reported behavior of *C. elegans* and our vinegar eel nematodes. These similarities include undulatory swimming, bordertaxis, and synchronization in the gait of clusters of organisms. We have not found descriptions of metachronal waves in concentrations of *C. elegans* or other nematodes in the literature nor have we seen metachronal waves in concentrations of *C. elegans* in our lab [29].

We briefly describe our experimental methods in II. Measurements of individual vinegar eels at low concentration are discussed in section III. We describe the behavior of high concentrations of vinegar eels in section IV. Models of metachronal waves in cilia and flagella have described these systems as a chain of interacting phase oscillators, where each phase describes the motion of a cilium or flagellum tip [13, 14]. In section V we adopt a similar approach and model our ensemble of vinegar eels with a chain of interacting oscillators, but each phase describes the motion of an eel’s head. A summary and discussion follows in section VI.

II. EXPERIMENTAL METHODS

We obtained our *T. aceti* nematode and yeast culture from an aquarium supply store, and we grow it at room temperature in a 1:1 mixture of water and food grade apple cider vinegar. A few slices of apple were added to the mixture as a food source for the yeast. After a few ml of the purchased culture is added to the vinegar and apple mixture, it takes a few weeks before large numbers of vinegar eels are visible by eye in the mixture. The vinegar eels congregate at the surface and crawl up the container walls.

To study the motion of the vinegar eels, we used a Krontech Chronos 1.4 high speed video camera at 1057

frames per second (fps) giving image frames with 1024×1280 pixels. To connect the video camera to a conventional stereo compound microscope under bright field illumination, we used a 0.5X reduction lens adapter that matches the C-mount of our camera. The other end of the adapter fits in the 23.2 mm diameter eyepiece holder of our microscope. Videos were taken using the X4 or X10 microscope objectives.

At each magnification, we made short videos of a calibration slide with a small ruler on it. Frames from these videos were used to measure the pixel scale, giving 315 mm/pixel and 838 mm/pixel at X4 and X10 magnification, respectively. The field of view is $1.22 \text{ mm} \times 1.53 \text{ mm}$ at X4 magnification and $3.25 \text{ mm} \times 4.06 \text{ mm}$ at X10 magnification.

We present two videos, both taken on Feb 26, 2020. The first video [34], denoted Video A, filmed at X10 magnification, is of the vinegar eels at low concentration. The second video [35], denoted Video B, is at higher concentration and was filmed at X4 magnification. To achieve high vinegar eel concentration, we placed about 10 ml of the vinegar eel culture in a test tube and then used a centrifuge (a few minutes at a few thousand rpm or about 1000 *g*) to concentrate the eels at the bottom. A pipette was then used to extract fluid from the bottom of the tube.

Each video views a drop of about 100 μ l of dilute vinegar containing vinegar eels that was deposited on a dry glass slide. The drop was not covered with a coverslip, so its surface is curved due to surface tension. The slides wet so the drop is not spherical. The outer edge of the drop where it touches the slide remains fixed due to surface tension. In both videos, the drop was about a cm in diameter. In Video B, we touched the edge of the drop with a metal pin a few times to pull and extend the drop radially outward. This increased the drop surface area on the slide and decreased its depth. This system is nearly two dimensional as the vinegar eels rarely swim above or below one another. Additional experiments of drops containing *T. aceti* are discussed by Peshkov et al. [29].

III. OBSERVATIONS OF LONE EELS AT LOW CONCENTRATION

In Video A, the vinegar eels are at low concentration and we can find intervals when an individual eel is not strongly influenced by nearby eels or borders. We focus on an adult $\sim 1 \text{ mm}$ long vinegar eel, shown in Figure 1, because it can be directly compared to prior work studying 1 mm long *C. elegans* kinematics (e.g., [31, 36, 37]) and because eels of this length actively participate in the metachronal wave.

A median image was subtracted from all frames in Video A to remove smooth variations in lighting. After subtracting the median image, we rotated the video frames so that the lone vinegar eel swims to the left. To find the eel’s oscillation or gait period we summed 5

TABLE I. Properties of a freely swimming vinegar eel

Quantity	Symbol	units	Value
Length	L	mm	0.96 ± 0.03
Diameter	w	mm	0.021 ± 0.001
Length/diameter	L/w	-	45
Wavelength	λ_u	mm	0.50 ± 0.02
Amplitude	A_u	mm	0.045 ± 0.005
Swim speed	v_{swim}	mm/s	0.38 ± 0.03
Amplitude/phys. length	A_u/h_x	-	0.055
Amplitude times wave-vector	$A_u k_u$	-	0.56
Oscillation period	T_u	ms	170 ± 6
Oscillation frequency	$f_u = 1/T_u$	Hz	5.9 ± 0.2
Undulation wave speed along body	$v_u = \lambda_u/T_u$	mm/s	3.0

The length h_x is the linear distance between head and tail measured along the direction of motion. The length L is that of the eel, integrated along its body or measured if it were extended to its maximum length. Because the eel is not straight while it is swimming $h_x < L$. The wave speed along the body is that of undulation. Uncertainties describe the range of values that would be consistent with the motion during a 1 s long segment of video. The vinegar eel is shown in Figure 1.

equally spaced (in time) video frames. We adjusted the time interval between the frames until the eel body shape was similar in each of the 5 frames, indicating that they are at about the same phase of undulation. This time interval gives us an estimate for the eel undulation period T_u . The sum of 5 images is shown in Figure 1a with the eel head on the left.

We estimated the eel's mean swim speed, v_{swim} by shifting the images so that the eel bodies in the 5 video frames appear to be at the same position. The required shift to align the eels after one oscillation period divided by the oscillation period T_u gives the mean swim speed, v_{swim} .

We used the mean swim speed to shift the video images so that positions are viewed in the reference frame moving with this average speed. At 9 different phases of oscillation during a single oscillation period, we measured eel body centerlines by fitting Gaussian functions to equally spaced vertical slices in the image. The mean of the Gaussian gives the eel's centerline y value as a function of horizontal distance x . The body centerlines at these 9 different phases of oscillation are shown with different colored dots in Figure 1b. The body centerlines are plotted on top of the first video frame in the sequence which is shown with the underlying grayscale image. In this figure, the origin is near the head's mean position. The positive x axis opposite to the swim direction and the y axis is perpendicular to it.

By integrating distances between the points along the eel's centerline, we computed the length L of the eel. We measured the eel's body diameter w by measuring its apparent width across its middle. In Figure 1b the horizontal extent of the eel h_x along the x axis is smaller than the eel length because the eel body is not straight.

To estimate a beat amplitude A_u and a wave vector k_u , we fit a sine wave to the body centerline at one phase

of oscillation

$$y(x) = A_u \cos(k_u x - \phi_0). \quad (1)$$

Figure 1c shows the fit sine function with a red line. The sine describes the y coordinate of the eel's centerline as a function of x and ϕ_0 is a phase. The wavelength of the body shape $\lambda_u = 2\pi/k_u$. The amplitude A_u describes the size of deviations from the mean of the centerline. The speed that waves travel down the body v_u is estimated from $v_u = \lambda_u/T_u$.

Measurements of the freely swimming vinegar eel are summarized in Table I. Uncertainties listed in this table give the range of values that are consistent with the eel's motion during a 1 s long segment of video.

The centerline positions in Figure 1b show that larger amplitude motions, or larger deviations from a pure sine shape occur at the head and tail of the vinegar eel. Over much of the body the eel's shape is well described with a sine function and the eel's body is nearly sinusoidal in shape during most of its oscillation. The spacing and offsets between centerline curves at different phases of oscillation in Figure 1b and c imply the advance of the sine shape occurs at a nearly constant wave speed.

Our vinegar eels culture contains nematodes of different sizes, ranging from about 0.3 to 2 mm in length (see Figure 2a). We measured the frequency of oscillation for different length eels and found that this frequency is not strongly dependent on eel length. We have noted that the ratio of length to wavelength L/λ_u is larger for the larger and longer eels than the smaller ones. In the longer eels about 1.5 wavelengths are present whereas only 1 wavelength is present on the shorter ones.

The key findings of this section are the measurement of the frequency of undulation for freely swimming vinegar eels ($f_u \sim 6$ Hz) and that the shape and motion of much of the vinegar eel's body can be described with a sine function.

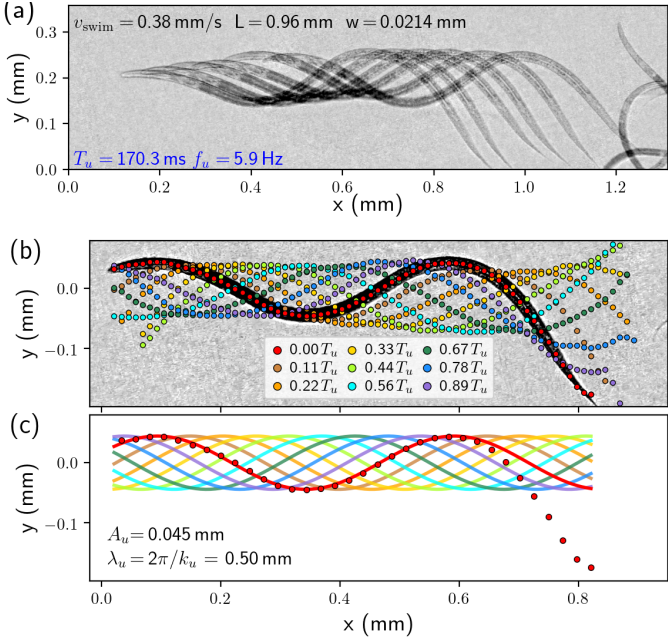


FIG. 1. Characteristics of an adult mm long freely-swimming vinegar eel. (a) The gray-scale image shows a sum of 5 frames from high speed Video A showing the same freely swimming eel. The 5 frames are equally spaced in time with interval $T_u = 170.3$ ms that is approximately one oscillation or undulation period. The oscillation frequency is written on the lower left in Hz; $f_u = 1/T_u$. The swim speed, v_{swim} , eel length, L and diameter w are written on the top of the frame. The images have been rotated so that the organism is swimming in the horizontal direction and to the left. (b) Body positions are shown with colored dots at 9 equally spaced times during a single oscillation period. The images used to measure the body position have been shifted to take into account the mean swim speed. The body positions are plotted on top of the first video frame in the sequence. (c) Using the first time shown in (b), the y position of the center of the eel body as a function of x is plotted with red dots enclosed in black circles. The red line shows the sine function $y = A_u \cos(k_u x - \phi_0)$ fit to these points. The wavelength and amplitude of this function are shown on the lower left. The colored lines show $y = A_u \cos(k_u x - \phi_0 - 2\pi j/9)$ for integers $j \in 1 \dots 8$ corresponding to the phases of oscillation shown in (b). The eel body is approximately sinusoidal in shape over much of its body and during most of its gait.

A. Comparison between *C. elegans* and *T. aceti*

Since the *C. elegans* nematode is well studied, we compare its kinematics to that of the vinegar eel nematode, *T. aceti*. The frequency of undulation we measured in the vinegar eels ~ 6 Hz is faster than the ~ 2 Hz measured in similar length (1 mm long) *C. elegans* [31, 36]. The length to diameter ratio for our 1 mm eel is about $L/w \sim 45$ whereas *C. elegans* is not as slender with $L/w \sim 12$ [36]. More than 1 wavelength fits within the eel body in *T. aceti*, particularly in the longer eels. In contrast about a single wavelength fits on the *C. elegans* body while it

is swimming [36]. The speed that waves travel down the body, $v_u \sim 3$ mm/s for the eel, is somewhat higher than that of *C. elegans* (2.1 mm/s, [36]). The swim speeds are similar; 0.4 mm/s for the 1 mm long vinegar eel and 0.36 mm/s in *C. elegans*.

In the vinegar eels, the amplitude of motion is larger at the head and tail, than in the middle and is largest at the tail. This behavior is similar to swimming *C. elegans* [31] (see their Figure 1a) though Sznitman et al. [36] measured the largest body curvature variations near the head.

For vinegar eels at low concentration, we did not find a significant difference between the undulation frequency of eels that are swimming near or along the edge of the drop and of those that are swimming in the center of a drop. In this respect our vinegar eels are similar to *C. elegans*. For *C. elegans* exhibiting bordertaxis and swimming near a surface, the frequency of oscillation is similar to that of the freely swimming organism [31].

IV. OBSERVATIONS OF METACHRONAL WAVES AT HIGH CONCENTRATIONS

At high concentration and a few minutes after the drop is placed on the slide, the eels collect near the edge of the drop, where the air/fluid boundary touches the slide, and just within the outer rim of the drop. Collective motion in the form of a traveling wave becomes progressively stronger and can be seen without magnification by eye as the vinegar eels are about 1 mm long (see Figure 2).

In Figures 2a and 3 we show frames from taken from Video B. The frames in Figure 3 have been rotated to orient the drop edge horizontally and at the bottom of each panel. To aid in comparing the frames at different times, we geometrically distorted each frame with a near identity quadratic coordinate transformation so as to make the boundary horizontal. The transformation used is $(x, y) \rightarrow (x, y - \frac{1}{2R_c}(x - x_c)^2)$ with x_c the x coordinate of the center of the image and R_c is a radius of curvature. Due to surface tension the actual drop edge is curved, with a radius of curvature of about $R_c \approx 7$ mm.

Using frames from the rotated and distorted video we created a time series of one dimensional arrays by integrating intensity along the vertical axis of the image. The vertical distance integrated is 1 mm and covers the frames in the series shown in Figure 3. This integration gives an intensity array $\rho(x, t)$ as a function of time t with x axis parallel to the drop edge. We use $\rho(x, t)$ to estimate the metachronal travel speed. We compute a correlation function, shown in Figure 4,

$$C(\Delta x, \Delta t) = \frac{\int dx \rho(x, t) \rho(x + \Delta x, t + \Delta t)}{\int dx \rho(x, t)^2}. \quad (2)$$

where Δx is a horizontal shift and Δt is a time delay. The ridges in Figure 4 are regions of higher intensity that propagate as a wave and their slope, shown with a

TABLE II. Metachronal wave measurements

Quantity	Symbol	Value
Metachronal wave velocity	v_{MW}	3.7 ± 0.2 mm/s
Metachronal wave frequency	f_{MW}	4.0 ± 0.2 Hz
Wavelength of metachronal wave	λ_{MW}	0.89 ± 0.03 mm
Number of eels per wavelength	N_{MW}	13-16
Ratio of frequencies	f_{MW}/f_u	~ 0.68
Amplitude of motion	A_{MW}	~ 0.07 mm

red segment, is the metachronal wave speed, v_{MW} . We estimate the metachronal wave speed by shearing the correlation function image until the ridges are vertical. The uncertainty in v_{MW} is estimated from the range of shear values that give vertical ridges upon visual inspection of the sheared correlation array. We estimate the metachronal wavelength λ_{MW} with a Fourier transform of the orientation angles array shown in Figure 6 (which is discussed in more detail below). The size of the error is based on the estimated covariance of a Gaussian fit to the Fourier transform. We checked that this wavelength was consistent with that measured from the distance between peaks in the correlation function shown in Figure 4. The wavelength and wave speed also give a metachronal wave oscillation frequency $f_{\text{MW}} = v_{\text{MW}}/\lambda_{\text{MW}}$. The measurements of the metachronal wave, v_{MW} , λ_{MW} , and f_{MW} , are listed in Table II.

Head positions for 4 eels were tracked by clicking on their head positions in two hundred frames spanning 2 seconds from Video B and their trajectories are shown in red in Figure 5. The eels don't swim forward very quickly. The four eels were chosen because their heads were easiest to identify during the 2 s video clip. The amplitude of back and forth motion for the eel heads is about $A_{\text{MW}} \sim 0.07$ mm. This amplitude is an estimate for the amplitude of motion for eels engaged in the metachronal wave and it exceeds the amplitude of motion $A_u \sim 0.045$ mm in the 1 mm long freely swimming eel.

By counting eel widths, we estimate that $N_{\text{MW}} = 13$ to 15 eels per metachronal wavelength λ_{MW} are involved in the traveling wave. However only about 8 eels per mm have heads visible near the edge of the drop. Some of the eel heads are more distant from the edge of the drop and are confined between other eel bodies. For deeper water/vinegar drops, the number of eels per unit length in the metachronal wave is sensitive to wetting angle [29].

The metachronal wave frequency $f_{\text{MW}} \sim 4 \pm 0.2$ Hz is significantly lower than the undulation frequency of individual freely swimming eels, $f_u \approx 6$ Hz. Studies of metachronal wave formation in cilia and flagellate bacteria have found that as the filaments or flagella enter a traveling wave state, their frequency of oscillation *increases* because hydrodynamic drag on the filaments is reduced when they are collectively beating in a wave pattern [13, 14]. However, here we find that the metachronal wave frequency is lower than that of the freely swimming eels. Since eels swimming along the edge of the drop

do not exhibit a lower undulation frequency, the reduced frequency must be due to interactions between organisms and we infer that interactions between neighboring eels reduce, rather than increase, their oscillation frequency.

A. Body orientations

Figure 3 suggests that when engaged in the metachronal wave, portions of the eel's bodies spend more time at some orientation angles than others. Figure 5 shows that during some phases of the wave, the eel heads move away from their neighbors. There are larger gaps between eels at some phases of the wave. These observations suggest there are deviations from sinusoidal motion. In this section we measure body orientations from the video frames to quantitatively examine this possibility.

To measure the local orientation of the eel bodies we compute local histograms of oriented gradients (HOG). These histograms are commonly used in object recognition software [38]. Figure 6 was made from one of the panels shown in Figure 3. In each 12x12 pixel square cell in the image, we computed histograms of oriented gradients with the `hog` routine that is part of the image processing python package `scikit-image`. We use unsigned gradients so orientation angles lie between $[-\pi/2, \pi/2]$. At each cell an average direction was computed using the histograms and these are plotted as blue segments on top of the original video frame in Figure 6a. In Figure 6b, the same blue segments are plotted on top of a color image with color showing the angles themselves. The color bar on the right relates orientation angle to color, with white corresponding to a horizontal orientation. In non-empty regions, we estimate an uncertainty less than $\pm 20^\circ$ in the orientational angles based on inspection of Figure 6a.

To examine statistical variations in the body orientations we computed distributions from the orientation angles (like those shown in Figure 6) but using 200 video frames from Video B spanning a duration of 2 s. A large number of video frames were used to average over the different phases of the wave. Orientation angle distributions are shown in Figure 7b.

Three rectangular regions are drawn in Figure 7a on one of the image frames and each region is plotted with the same color and thickness line as used in Figure 7b. In Figure 7b we show distributions of orientation an-

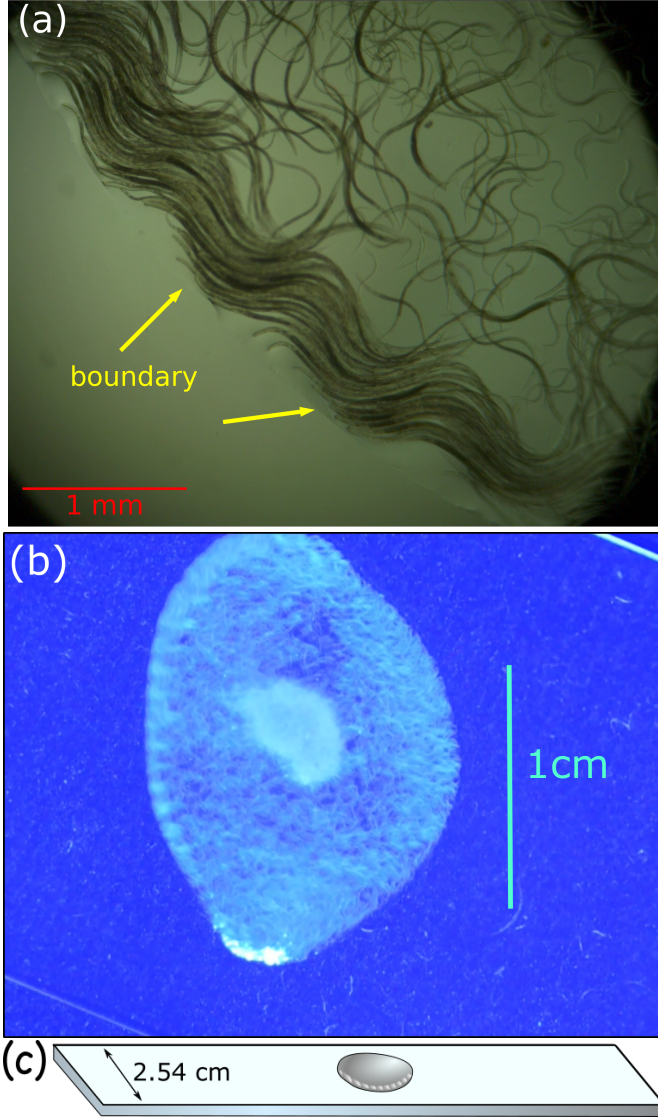


FIG. 2. (a) A raw video frame from Video B. This video is of a dilute vinegar drop containing a high concentration of vinegar eels seen through a conventional microscope at X4 magnification. The edge of the drop on the slide is marked with yellow arrows. The concentration of eels is higher near the edge of the drop. There are eels of different lengths and ages in the solution, however the smaller eels are less likely to participate in the metachronal wave. (b) A photograph taken from above of a drop on a slide containing a high concentration of vinegar eels. Detritus in the culture has been pushed to the center of the drop. The feathery white ridges on the edge of the drop are the metachronal wave. (c) An illustration of the drop of concentrated vinegar eel solution on a slide. The white feathery features represent the traveling wave in the vinegar eels near the edge of the drop.

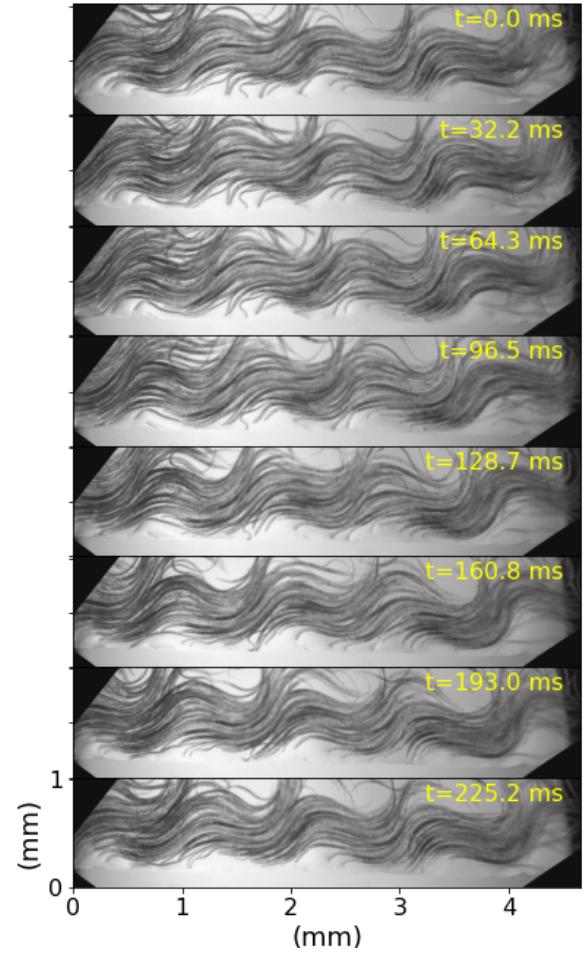


FIG. 3. Each panel show the same subregion of a series of frames from Video B. The edge of the drop is near the bottom of each panel. The time of each frame from the beginning of the sequence is shown in yellow on the top right of each panel. The x and y axes are in mm.

gles measured in these three rectangular regions. The three region centers have different distances from the edge of the drop, 0.47, 0.29 and 0.13 mm. The higher color opacity lines in Figure 7b are distributions computed with weights so that regions of high eel intensity contribute more to the histogram. The lighter and lower opacity lines are distributions computed without weighting. The difference between the higher and lower opacity lines shows that the orientation angle distributions are not sensitive to local variations in image intensity. The red rectangular region (plotted with wider lines) is more distant from the edge of the drop than the blue region. The red histogram is wider than the blue one, indicating that there is a wider range of body orientation angles more distant from the drop edge.

The distributions shown in Figure 7b have a trough and are asymmetric or lopsided, with one peak higher than the other. This asymmetry is not expected as a sine wave has distribution of orientations (computed

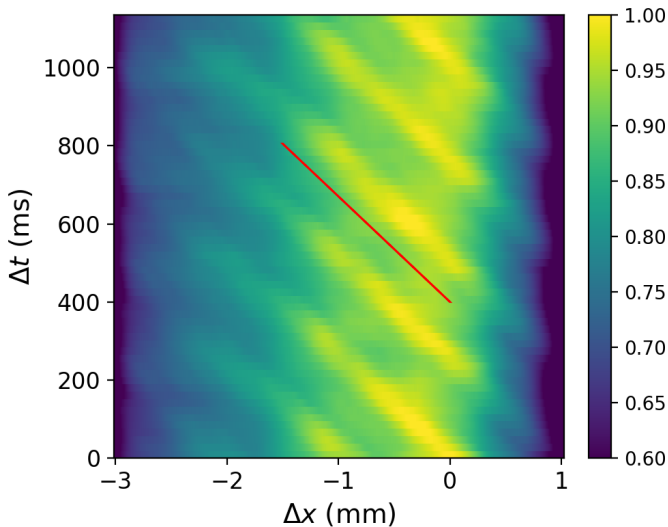


FIG. 4. Correlation function computed using equation 2 from image intensity as a function of spatial shift Δx and time delay Δt . The metachronal wave speed depends on the slope of the ridges. The estimated metachronal wave speed of $v_{MW} = 3.7$ mm/s is shown with the red segment.

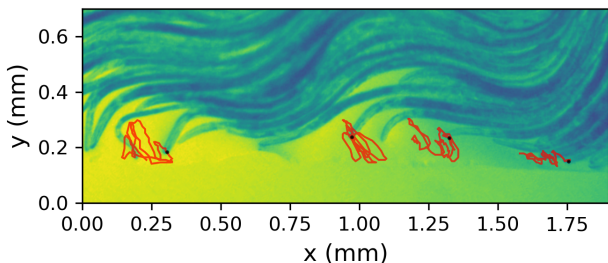


FIG. 5. Head positions for 4 eels were tracked over 2 seconds of video and their trajectories are shown in red on the image. The black dots show the location of the eel heads at the same time as the video frame. The eels don't advance forward very quickly or at all while they are engaged in the metachronal wave. The amplitude of back and forth motion is about $A_{MW} \sim 0.07$ mm, and exceeds that of the freely swimming eel.

from its slope) that would be symmetrical about a mean value. Models for the orientation angle distribution are discussed further in section V D.

In summary, we find that for vinegar eels engaged in a metachronal wave, the distribution of body orientation angles has two peaks of different heights and depends on distance to the drop edge. The asymmetry in the orientation angle distribution and inspection of eel heads near the drop edge implies that eel body shapes and motions are not perfectly sinusoidal. This contrasts with our study of the freely swimming eels in section III where we found that the shape and motion of freely swimming eels is nearly sinusoidal.

V. OSCILLATOR MODELS FOR TRAVELING WAVES

Experimental observations have shown that motility of swimming nematodes, such as *C. elegans*, is due to the propagation of bending waves along the nematode's body length [39]; (for a summary of nematode locomotion neurobiology, see [40]). The bending waves consist of alternating phases of coordinated dorsal and ventral muscle contractions and extensions [41]. During locomotion, motor neurons excite muscles on either (ventral/dorsal) side of the body while inhibiting muscles on the opposite side.

The gait of *C. elegans* adapts to the mechanical load imposed by the environment [42]. Swimming involves higher frequency and longer wavelength undulations than crawling on agar, though both behaviors may be part of a continuous spectrum of neural control [43, 44]. Oscillation frequencies also decrease for *C. elegans* swimming in higher viscosity aqueous media [36]. Proprioception is when sensory receptors in muscles or other tissues are sensitive to the motion or position of the body. In models for nematode locomotion, the sensitivity to environment involves proprioceptive integration or feedback on the neuronal control model [37, 40, 43, 45].

Experiments of restrained *C. elegans* [37] show that the bending of the posterior regions requires anterior bending (see Figure 3 by Wen et al. [37]). If the nematode is held fixed at its middle, the body can undulate between head and constraint, but past the constraint to the tail, there will be no undulation. These experiments suggest that the body itself lacks central pattern generating circuits and motivates locomotion models that rely on an oscillator in the head [37].

To create a model for collective motion in the vinegar eels, we assume that the waves that propagate down the nematode's body are initiated at the organism's head. We use the phase of the head's back and forth motion with respect to its mean position to describe the state of each organism and we model our ensemble of eels as a chain of phase oscillators. In the absence of interactions, each oscillator has intrinsic frequency equal to the oscillation frequency of a freely swimming eel. Because the mean positions (averaged over the oscillation period) of the eel's heads drift very slowly (see Figure 5), we neglect drift in the mean or averaged (over a period) oscillator positions. Here the oscillator phase is associated with back and forth motion of an eel head because the head is assumed to be the source of the body wave. This differs from the models by Niedermayer et al. [13], Brumley et al. [14] where the phase describes motions of a cilium or flagellum tip.

When the vinegar eels are engaged in metachronal waves, the organisms are often touching each other. Chelakkot et al. [21] simulated steric interactions between active and elastic filaments in arrays and found that short-ranged steric inter-filament interactions can account for formation of collective patterns such as

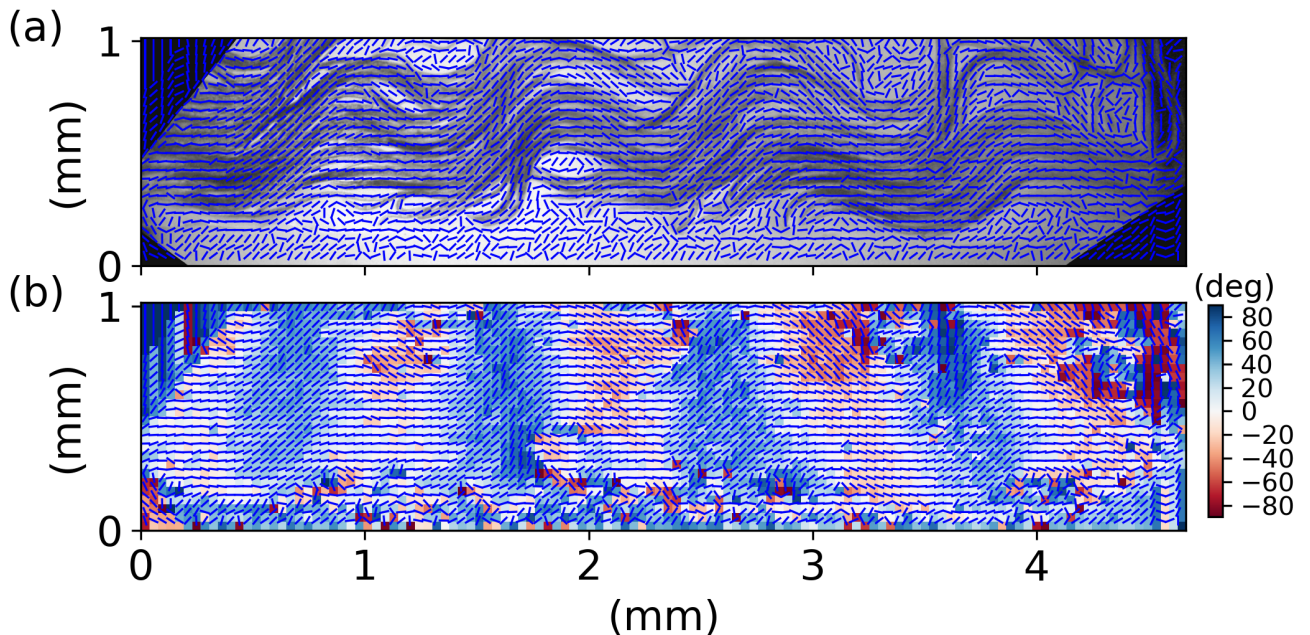


FIG. 6. Body orientation angles. In (a) and (b) panels the blue segments are oriented with the means of locally computed histograms of oriented gradients. The histograms of oriented gradients were computed from one of the images in Figure 3 from Video B. The same image is shown in gray-scale in panel (a). The color image in panel (b) displays the orientation angles, with color-bar on the right in degrees.

metachronal waves. Because undulation frequency of *C. elegans* is slower when under mechanical load imposed by the environment, we assume that steric interactions in our vinegar eels reduce the phase velocity of oscillation.

To construct a model for metachronal waves, we consider the head of a single organism to be an oscillator and we consider ensembles of N oscillators. The i -th oscillator can be described with a phase θ_i and a frequency of oscillation or a phase velocity $\frac{d\theta_i}{dt} = \dot{\theta}_i$. Here i is an integer index and θ_i is a function of time t .

Collective phenomena involving synchronization of oscillators has been described with different nomenclature. Following [13, 46], a *synchronized* state of an ensemble of N oscillators is one where all oscillators have identical phases, $\theta_i(t) = \theta_j(t)$ for all $i, j \in (0, 1, \dots, N-1)$. A *phase-locked* or *frequency synchronized* state [22–24] is one where all oscillators have identical phase velocities $\dot{\theta}_i(t) = \dot{\theta}_j(t)$ for all $i, j \in (0, 1, \dots, N-1)$. An *entrained* state has identical mean phase velocities $\bar{\omega}_i = \bar{\omega}_j$ for all $i, j \in (0, 1, \dots, N-1)$. The time average of the phase velocity can be computed with an integral over time, $\bar{\omega}_i = \lim_{t \rightarrow \infty} \frac{1}{t} \int_0^t \dot{\theta}_i(t) dt$, or by integrating over an oscillation period if oscillator motions become periodic.

For a chain of oscillators, the index i specifies the order in the chain. One type of traveling wave is a non-synchronous phase-locked state characterized by a constant phase delay or offset between consecutive oscillators in a chain or loop of oscillators. In other words $\theta_{i+1} = \theta_i + \chi$ for consecutive oscillators, where χ is the

phase delay and $\dot{\theta}_i \neq 0$ for all i . If individual oscillators undergo similar periodic motions, then another type of traveling wave is a non-synchronous but entrained state characterized by a time delay between the motions of consecutive oscillators. In other words $\theta_i(t + \tau) = \theta_{i+1}(t)$ with time delay τ . In this case the phase velocities would be periodic and need not be constant. Both types of traveling waves involve periodic oscillator motions and are known in the biological literature as metachronal waves.

A. Local Kuramoto models

The Kuramoto model [46–48] consists of N oscillators, that mutually interact via a sinusoidal interaction term

$$\frac{d\theta_i}{dt} = \omega_i + \sum_{j=1}^N K_{ij} \sin(\theta_j - \theta_i) \quad (3)$$

where K_{ij} are non-negative coefficients giving the strength of the interaction between a pair of oscillators. In the absence of interaction, the i -th oscillator would have a constant phase velocity ω_i which is called its intrinsic frequency.

With only nearest neighbor interactions a well studied model, sometimes called a local Kuramoto model, is described by

$$\frac{d\theta_i}{dt} = \omega_i + K [\sin(\theta_{i+1} - \theta_i) + \sin(\theta_{i-1} - \theta_i)] \quad (4)$$

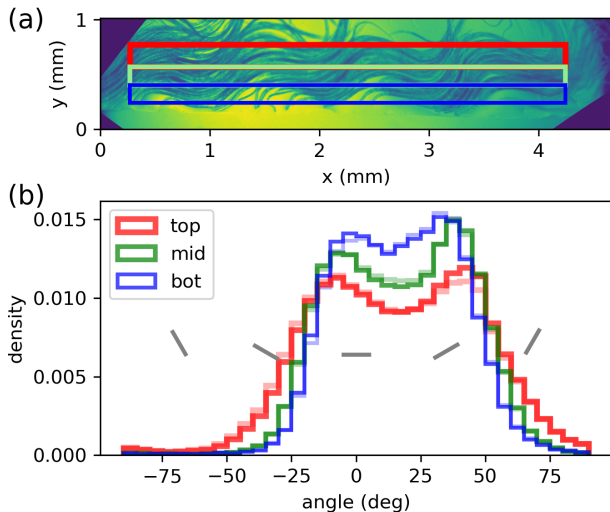


FIG. 7. Distributions of orientation angles in the metachronal wave. (a) Three rectangular regions are shown on top of one of the image frames. The color and line width showing each region is the same as in panel (b). (b) Normalized distributions of orientation angles in the three rectangular image regions. The histograms were computed using orientations like those shown in Figure 6, but using 200 video frames from Video B spanning a duration of 2 s. The higher opacity lines are histograms computed with intensity weights with regions of higher eel density contributing more to the histogram. The lighter lines are histograms computed without weighting. The distribution is narrower near the edge of the drop. The gray bars have orientation equivalent to their x coordinates on the plot and are plotted at multiples of 30° . The difference in the two peak heights in each distribution suggest that there are deviations from sinusoidal shapes and motions.

[22–27]. At low values of positive interaction parameter K , the oscillators are not affected by their neighbors. At higher K , the oscillators cluster in phase velocity, and the number of clusters decreases until they fuse into a single cluster that spans the system. At and above a critical value of $K = K_s$ the entire system must enter a global phase-locked state [49]. Above the critical value $K > K_s$, there can be multiple stable phase-locked attractors, each with its own value of global rotation rate $\Omega = \frac{1}{N} \sum_i \omega_i$ [26, 50].

What fraction of possible initial conditions would converge onto a phase-locked solution that is not synchronous? The set of initial conditions that converge onto a particular solution are called its *basin of attraction*. The basins of attraction for traveling wave solutions (or non-synchronous phase-locked states) are smaller than that of the synchronous state [26, 27]. Using random and uniformly generated initial phases in 0 to 2π for each oscillator, the system is more likely to enter a synchronous rather than a traveling wave state.

Because well studied local Kuramoto models like that of equation 4 are more likely to enter a synchronous than a traveling wave state, they do not capture the behavior illustrated by our vinegar eels, or other systems that

exhibit metachronal waves such as chains of cilia [13] or flagella on the surface of *Volvox carteri* alga colonies [14]. Relevant models should exhibit a larger basin of attraction for traveling wave states than for the synchronous state.

In models for metachronal waves in cilia or flagellates [13, 14, 18] the end of a filament moves in a plane and on a trajectory of radius R from a central position with phase θ in polar coordinates. Active forces are induced via tangential forces exerted on the filament. Interactions between the oscillators are based on hydrodynamic interactions between pairs of filaments and are computed using Stokes equation which is valid at low Reynolds number [8, 13, 14, 18]. Motion is over-damped so the equations of motion are a balance between driving and hydrodynamic forces. The filament velocities are computed as a function of their positions and it is not necessary to compute accelerations. The equations of motion describe motions of the phase, radius and orientation angle of the end of the filament’s trajectory. However, if the distance between filaments is large compared to the radius of motion, the dynamical system can be approximated with nearest neighbor interactions and neglecting variations in the radius or plane of motion [13]. This gives a local oscillator chain model dependent only on phases.

B. An oscillator model based on heads that overlap

We desire a model that has a wide basin of attraction for traveling wave states, similar to those by Niedermayer et al. [13], Brumley et al. [14]. The oscillator chain model by Niedermayer et al. [13] included sine and cosine terms of the sums and differences of pairs of phases and that by Brumley et al. [14] included both radial and phase motions. We can similarly assume that motion is over-damped and can be described by equations for phase and phase velocity and lacking phase accelerations. Since steric interactions are likely to be important, we can adopt a model with only nearest neighbor interactions, as did Niedermayer et al. [13]. However, opposite to the hydrodynamic interaction models, the interactions between our eels are likely to be strong, and they should reduce the oscillator phase velocity rather than increase it. We observe that eel heads near the edge of the drop (see Figures 3, 5) were not near other eel bodies during portions of the traveling wave. If undulation is generated at the eel head, then interactions on it are only strong during about half of the head’s oscillation cycle.

Consider two eels oriented horizontally as shown Figure 8a with x the horizontal axis and y the vertical one. The eels undulate with amplitude A and without varying the head’s x position or the orientation of its mean centerline, which is shown with dotted lines. The y position of the i -th head

$$y_i = A \cos \theta_i - id, \quad (5)$$

where d is the distance between the neighboring eel’s

mean centerlines. The phase of oscillation is given by the angle θ_i . The distance between the two heads with index i and $i-1$ is

$$\Delta_{\text{left}} = d + A \cos \theta_i - A \cos \theta_{i-1}. \quad (6)$$

The eels with index i and $i-1$ overlap near their heads if the left-sided overlap function

$$o_{\text{left}}(\theta_{i-1}, \theta_i) = \frac{\Delta_{\text{left}}}{A} = \cos \theta_i - \cos \theta_{i-1} + \beta < 0, \quad (7)$$

where the dimensionless overlap parameter

$$\beta \equiv \frac{d}{A}. \quad (8)$$

We assume that a strong steric interaction on the i -th eel's head would reduce its phase velocity when $o_{\text{left}}(\theta_{i-1}, \theta_i) < 0$. Otherwise, the eel head's phase velocity would remain at its intrinsic phase velocity. Because the eels tend to be closer together than the amplitude of undulation when they are involved in a metachronal wave, we expect β to be smaller than 1. The amplitude A of body motions for eels engaged in the metachronal wave need not be the same as that of the freely swimming eel, A_u .

Consider three eels oriented at an angle as shown in Figure 8b. The oscillator in the i -th eel's head is more strongly influenced by the motions of the organism to its left (with index $i-1$) and less so by the one to its right (with index $i+1$). When the eels are tilted with respect to the edge of the drop, we expect directed interactions where the phase of the eel's head is primarily influenced by its nearest neighbor on one side.

A modification to the local Kuramoto model with directed or one-sided nearest neighbor interactions

$$\frac{d\theta_i}{dt} \omega_0^{-1} = 1 - K f(\theta_{i-1}, \theta_i). \quad (9)$$

Here positive and dimensionless parameter K describes the strength of the interaction. The nearest neighbor interaction function $0 < f(\theta_{i-1}, \theta_i) \leq 1$, reduces the phase velocity and mimics the role of one-sided steric interactions. The intrinsic angular phase velocity ω_0 is the same for each oscillator. We work with time in units of ω_0^{-1} which is equivalent to setting $\omega_0 = 1$.

One choice for the interaction function should give 1 if the overlap function o_{left} (defined in equation 7) is negative and there is an overlap and gives 0 otherwise. This choice neglects eel body width. We have checked with numerical integrations that a numerical model based on a Heaviside step function can robustly give traveling wave solutions. However, numerical integration of a discontinuous function with a conventional numerical integrator can give results that are dependent on step size or sensitive to round-off or discretization errors. To mitigate this problem we use a smooth function to approximate the step function, $f(\theta_{i-1}, \theta_i) = \frac{1}{2} \left[1 - \tanh \frac{o_{\text{left}}(\theta_{i-1}, \theta_i)}{h_{ol}} \right]$

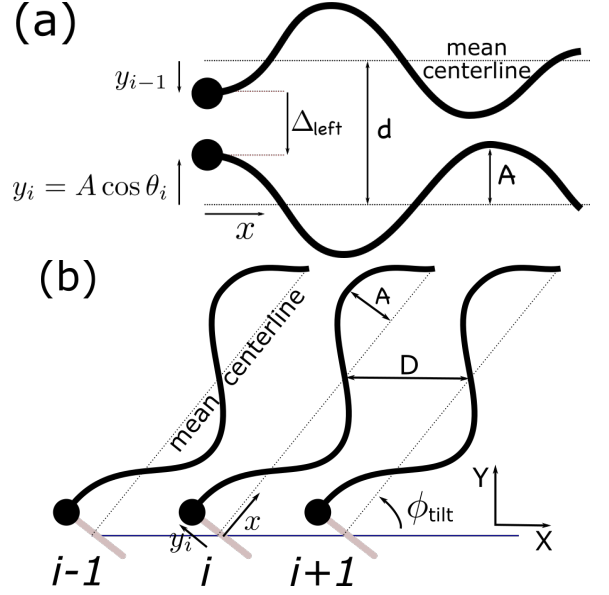


FIG. 8. (a) Two eels undulate with amplitude A but without moving their mean centerlines. The two mean centerlines are shown with dotted lines and are separated by distance d . The eel heads are shown with large black dots. We assume that the undulation on the body is initiated by oscillators in the eel's heads. The oscillators have phases θ_i and θ_{i-1} . When $\Delta_{\text{left}} = d + A \cos \theta_i - A \cos \theta_{i-1} < 0$, the eel heads overlap and steric interaction would slow their motion. (b) Three consecutive eels are tilted by angle ϕ_{tilt} with respect to the horizontal direction. The oscillator in the i -th eel's head is more strongly influenced by the motions of the organism to its left (with index $i-1$) than the one to its right (with index $i+1$). At lower tilt angle ϕ_{tilt} , the interactions are increasingly lopsided.

where dimensionless parameter h_{ol} sets the abruptness of the transition of the function from 0 to 1. In the limit of small h_{ol} we recover the Heaviside function. An oscillator model that uses this smooth function has equation of motion

$$\frac{d\theta_i}{dt} \omega_0^{-1} = 1 - \frac{K}{2} \left[\tanh \left(\frac{\cos \theta_{i-1} - \cos \theta_i - \beta}{h_{ol}} \right) + 1 \right]. \quad (10)$$

C. Numerical integrations of a directed overlap phase oscillator chain model

The directed overlap phase oscillator model given by equation 10 depends on three positive parameters, the interaction strength K , an overlap parameter β and the parameter setting the smoothness of the interaction function h_{ol} . The model is also sensitive to the number of oscillators in the chain or loop N , the boundary condition and the choice of initial conditions. We integrate this model using a first order explicit Euler method. The initial phases for each oscillator are randomly generated using a uniform distribution spanning $[0, 2\pi]$.

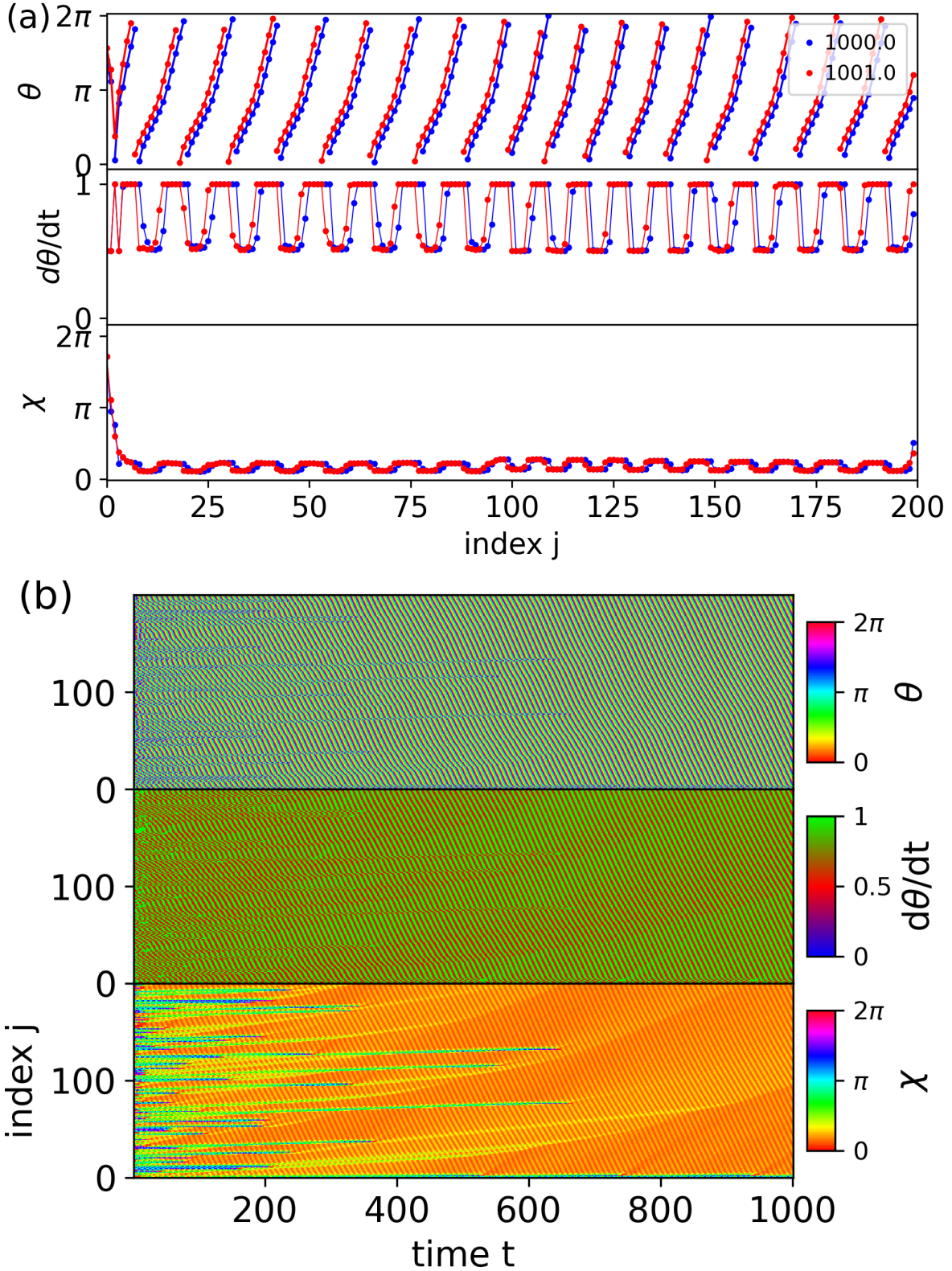


FIG. 9. A directed oscillator chain model numerical integration. Equation 10 is integrated with $N = 200$ oscillators in a chain with a non-periodic boundary condition and randomly chosen initial phases. The interaction parameter $K = 0.5$, intrinsic frequency $\omega_0 = 1$, overlap parameter $\beta = 0.25$, smoothness parameter $h_{ol} = 0.05$ and time-step $dt = 0.05$. The system was integrated to time $t = 1001$. At the end of this integration the average phase velocity $\bar{\omega} = 0.77\omega_0$ and the average wavelength is $N_\lambda = 12$ oscillators. (a) From top to bottom panels, the phase angles θ_j , phase velocity $d\theta_j/dt$ and phase difference $\chi_j = \theta_{j+1} - \theta_j$ are plotted as a function of index j at two different times. The outputs at $t = 1000$ and $t = 10001$ are plotted with red and blue lines. Comparison between these two outputs shows that they are similar but shifted by a time delay. The system is an entrained state which can also be described as a traveling wave state. (b) From top to bottom panels, the images show phase angle θ_j , phase velocity $d\theta_j/dt$ and phase difference χ_j with color shown in the color-bars on the right. The horizontal axes is time and the vertical axes are the oscillator index j . The fine diagonal features at large times are the traveling waves. The horizontal features are discontinuities that eventually disappear as coherent regions merge.

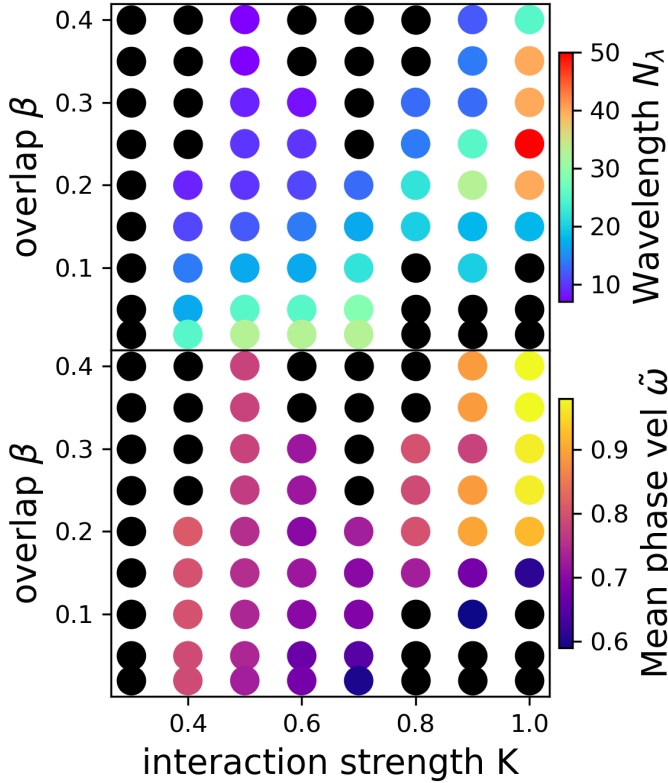


FIG. 10. Wavelengths N_λ and mean phase velocity $\tilde{\omega}$ computed for numerical integrations at $t = 1000$ of the directed oscillator chain model given in equation 10. The integrations have $N = 200$ oscillators, the timestep is $dt = 0.05$ the smoothness parameter is $h_{ol} = 0.1$, the boundary is not periodic and initial phases were randomly chosen. If the entire chain of oscillators did not reach a traveling wave state at $t = 1000$, a black dot is plotted otherwise the dot has color giving the wavelength N_λ (top panel) and mean phase velocity $\tilde{\omega}$ (bottom panel). The x axis is the interaction strength parameter K and the y axes are the overlap parameter β .

In local Kuramoto models, stable solutions that are present in a loop may not be present if one link is dissolved and the loop becomes a chain [26, 51]. To ensure that traveling waves are robustly generated in our model, we purposely do not chose a periodic boundary condition. The boundary at the end of the chain or for θ_{N-1} does not affect the dynamics because of the direction of the interactions. For the left boundary (with phase θ_0) we set the phase velocity $\frac{d\theta_0}{dt} = (1 - K)\omega_0$. We find that a slow left boundary is less likely to excite perturbations that propagate through the system.

A numerical integration with $N = 200$ oscillators, intrinsic frequency $\omega_0 = 1$, interaction parameter $K = 0.5$, overlap parameter $\beta = 0.25$, and smoothness parameter $h_{ol} = 0.05$ is shown in Figure 9. The time step used is $dt = 0.05$ and we have checked that a smaller step size does not significantly change the integration output. In Figure 9a the panels show phase angle θ_j , phase velocity $d\theta_j/dt$ and phase shift $\chi_j = \theta_{j+1} - \theta_j$ as a function

of index j for an integration at two times $t = 1000$ and $t = 1001$. In Figure 9b we show the same quantities but with color arrays as a function of both index and time. Despite the absence of a diffusive-like interaction term (similar to that in equation 4), the model has attracting entrained or traveling wave solutions. A comparison between the two outputs in the top panel shows that phases at different times can be related with a time delay. At the beginning of the integration clusters of entrained or nearly phase-locked groups form and later merge to give a fully entrained or traveling wave state. This type of behavior was previously seen in the oscillator models developed for hydrodynamic interactions between cilia and flagella [13, 14].

When initial conditions are random, there are initially groups of neighboring oscillators with large phase differences and these large differences can remain on the same group of oscillators for many oscillation periods. These are nearly horizontal streaks seen in the bottom panel showing phase difference χ in Figure 9b. Had we added a diffusive-like term to our model, small wavelength perturbations would be more rapidly damped, but such a term would also affect the velocity and wavelength of traveling wave states.

We ran the integration to a maximum time $t = 1001$ with $\omega_0 = 1$ corresponding to $1001/(2\pi) \approx 160$ oscillation periods ($2\pi/\omega_0$). For an oscillation frequency of $f_u \sim 6$ Hz (as we observed for our vinegar eels) this duration corresponds to 27 seconds. The metachronal waves take a few minutes appear after the drop is placed on the slide. The time it takes for all entrained clusters to merge in the numerical model is shorter than the few minutes it takes for traveling waves to form on a large portion of the drop edge in our concentrated eel experiments. However, our model is of a fixed chain of oscillators so it does not take into account the time it takes for the vinegar eels to collect on the boundary or sources of noise in the system.

At the end of the numerical integration shown in Figure 9, the average phase velocity $\tilde{\omega} = 0.77\omega_0$ (computed from all oscillators at that time), the average wavelength is $N_\lambda = 12$ oscillators. The phase delay for the entrained state $\tau = \frac{2\pi}{\tilde{\omega}N_\lambda} = 0.68$. The number of oscillators for a change of 2π in phase, N_λ , is comparable to that we estimated for the metachronal wave in the vinegar eels (see Table II). The average phase velocity ratio $\tilde{\omega}/\omega_0$ is near but somewhat higher than the ratio of metachronal wave to freely swimming undulation frequency $f_{MW}/f_u \sim 0.67$ that we estimated for the vinegar eels (listed in Table II and discussed in section IV).

If all phases are initially set to the same value, the dynamical system described by equation 10 remains in a synchronous state. However, if some noise is introduced into the system (in the form of small stochastic perturbations on each oscillator) then the system is likely to enter the traveling wave state even with flat initial conditions. The basin of attraction for the traveling wave state is significantly larger than that of the synchronous state.

With a fixed value of smoothness parameter h_{ol} , we integrated equation 10 for different values of interaction parameter K and overlap parameter β . These integrations have random initial conditions and non-periodic boundary, as described above, intrinsic frequency $\omega_0 = 1$ and smoothness parameter $h_{ol} = 0.1$. At $t = 1000$ we inspected plots like those in Figure 9 to see if the system was in an entrained state. If so, we measured the mean wavelength N_λ and the mean phase velocity $\tilde{\omega}$. In Figure 10 points are plotted as a function of β and K and with color set by their wavelength N_λ (top panel) or mean phase velocity $\tilde{\omega}$ (bottom panel). Systems that exhibited discontinuities at the end of the simulation (other than at the left boundary) are plotted in black. A fairly wide range of interaction and overlap parameters robustly gives entrained or traveling wave states.

At larger overlap parameter, β , the oscillators spend less time overlapped and this tends to give a shorter wavelength and higher mean phase velocity $\tilde{\omega}$ in the entrained state. If eels are more distant from each other or have lower amplitude oscillations then β is larger. At large overlap parameters $\beta \gtrsim 0.4$ (on the top of each panel in Figure 10) the system is less likely to be in a traveling wave state at $t = 1000$. This is due to clusters of oscillators that begin with large phase differences between neighbors that do not dissipate. High eel concentration would reduce the overlap parameter β , so the model does account for the sensitivity of the metachronal wave to eel concentration on the boundary.

Figure 10 shows that for $K < 0.4$ (on the left side of the figure) entrained states are not present at the end of the integration. This is due to groups of neighboring oscillators with initially large phase differences. If integrated longer, these irregularities or discontinuities might eventually disappear. The interaction parameter K influences the time it takes for the short wavelength structure to dissipate. In a more realistic model, noise and diffusive interactions would also affect the range of parameters giving an entrained or traveling wave state. The odd black points at $\beta \approx 0.25, K = 0.7$ are due to discontinuities at the left boundary that continuously propagate through the system. We are not sure why our left boundary condition caused this problem only in this region of parameter space.

What properties of a phase oscillator model are required for a large basin of attraction to an entrained or traveling wave state? The model by Brumley et al. [14] is two dimensional as it depends on oscillator radius as well as phase so it is more complex than a model that consists only of a chain of phases. With only phases, both our model and that by Niedermayer et al. [13] are not potential models, and interactions between pairs of oscillators are not applied equally and oppositely to each oscillator in a pair, the way conventional physical forces are applied. These three examples (our model, and those by Niedermayer et al. [13], Brumley et al. [14]) of models developed for traveling waves in biological systems might yield clues for more general classification of the basins of

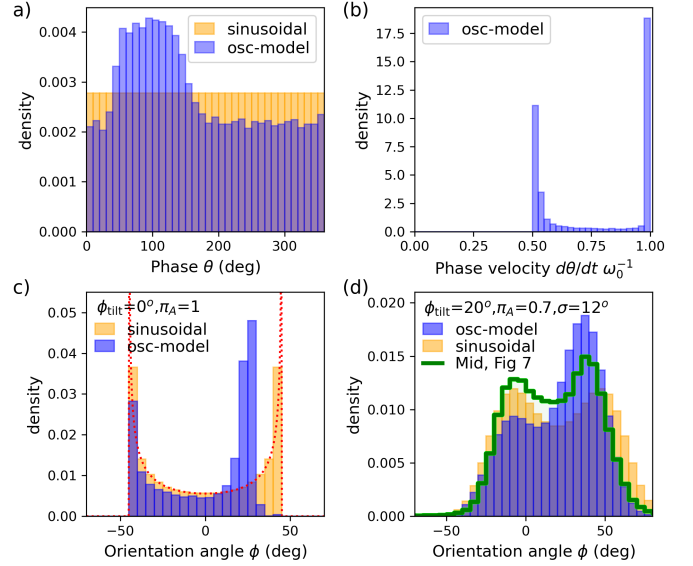


FIG. 11. Distributions for the directed chain integrated oscillator chain model shown in Figure 9 are plotted in blue. These are compared to distributions for a constant phase velocity model which is shown in orange and referred to as ‘sinusoidal’. (a) The distribution of phase angles for the integrated oscillator chain model and the sinusoidal model. (b) The distribution of phase velocities for the integrated oscillator chain model. The sinusoidal model has $d\theta/dt \omega_0^{-1} = 1$. (c) The distribution of orientation angles for both oscillator chain and sinusoidal models computed using equation 15, $\phi_{\text{tilt}} = 0$ and $\pi_A = A\omega_0/v = 1$. The red dotted line shows the distribution function (in equation 17) for the sinusoidal model. (d) We show smoothed distributions of orientation angles computed using equation 15, $\phi_{\text{tilt}} = 20^\circ$ and $\pi_A = 0.7$ for both oscillator chain and sinusoidal models. The sinusoidal and oscillator chain model distributions have been smoothed with a Gaussian filter with a standard deviation of $\sigma = 12^\circ$. With a thick green line, we show the distribution of orientations measured from the vinegar eels in Video B. This distribution is the same as plotted in green in Figure 7b. The directed chain oscillator model displays an asymmetry in the associated orientation angle distributions (i.e., peaks of different heights) that is present in the observed distribution.

attraction for phase oscillator models with local interactions.

For most of our integration parameters we saw only a single possible entrained state. Is it possible to predict the phase delay τ , or wavelength, N_λ , of this entrained state? The integration shown in Figure 9a of the model given by Equation 10 shows that the phase at a single output time has two regions. One region has a low phase velocity and the other region has a higher phase velocity. In the fast and slow regions, the phase velocity is constant and phase differences between neighboring oscillators are maintained. In appendix A, we estimate the phase delay τ and wavelength N_λ of the entrained state from the phase shifts that occur during the transitions between the fast and slow regions.

D. Distributions of orientation angles

How do we relate the oscillator chain model to the orientation distributions displayed in Figure 7b for the vinegar eels engaged in a metachronal wave? The undulation velocity we measured in the freely swimming eel $v_u \sim 3.0$ mm/s is similar to the metachronal wave velocity $v_{\text{MW}} \sim 3.7$ mm/s so we could use either one to make an estimate for how motions of the head propagate to the rest of the body. The free eel undulation frequency of $f_u = 5.9$ Hz gives intrinsic phase velocity $\omega_0 = 2\pi f_u = 37$ s⁻¹. It is useful to compute the dimensionless ratio

$$\pi_{A,\text{MW}} \equiv \frac{A_{\text{MW}}\omega_0}{v_{\text{MW}}} \approx 0.70 \quad (11)$$

using parameters listed in Table I and Table II that we measured for the freely swimming eel and metachronal wave.

The phase θ in our oscillator model represents the phase of back and forth oscillation in an eel's head. We constructed our interaction function assuming that the eel head moves away from its mean centerline with coordinate perpendicular to the mean centerline $y = A \cos \theta$. We assume that the head's motion excites a constant velocity traveling wave along the eel body $y(x, t)$ with distance y from the mean centerline a function of distance x along the mean centerline. The head's motion gives boundary condition

$$y(x = 0, t) = A \cos [\theta(t)], \quad (12)$$

where the function $\theta(t)$ gives the phase of the head oscillation as a function of time. With constant undulation wave velocity v

$$y(x, t) = A \cos \left[\theta \left(t - \frac{x}{v} \right) \right] \quad (13)$$

is consistent with the boundary condition at $x = 0$ (equation 12). The velocity that waves propagate down the eel body v may not be the same as v_u , the wave velocity for the freely swimming eel.

The slope of the body

$$\frac{dy(x, t)}{dx} = A \sin \left[\theta \left(t - \frac{x}{v} \right) \right] \theta' \left(t - \frac{x}{v} \right) v^{-1}. \quad (14)$$

Here θ' is the derivative of the function $\theta(t)$. The distribution of the slopes should be the same as the distribution of $\frac{A}{v} \frac{d\theta}{dt} \sin \theta$ where the phases θ and phase velocities $\dot{\theta}$ are those at different times and positions for the heads in the oscillator array after the integration achieves an entrained state. The slope of the body is $\frac{dy}{dx} = \tan \phi$ where ϕ is the body orientation angle. From our model phases and phase velocities we can compute the distribution of body orientation angles ϕ assuming a constant wave velocity v with

$$\phi = \arctan \left[\pi_A \left(\frac{d\theta}{dt} \frac{1}{\omega_0} \right) \sin \theta \right] + \phi_{\text{tilt}}, \quad (15)$$

with

$$\pi_A \equiv \frac{A\omega_0}{v}. \quad (16)$$

We have purposely written equation 15 in terms of dimensionless parameters so as to facilitate comparison of our model with the vinegar eel collective motions. Here the tilt angle ϕ_{tilt} , illustrated in Figure 8, lets us adjust the angle of the eel centerlines with respect to the drop edge.

We generate model orientation distributions for the oscillator chain model with parameters and integration shown in Figure 9. In Figure 11 we use the arrays from 20 different times (spaced at 0.5 duration intervals) to compute the distributions of phase angle θ , phase velocity $\frac{d\theta}{dt}$, and orientation angle ϕ . The orientation angles are computed with equation 15 from the phases and phase velocities. The distributions have been normalized so that they integrate to 1. For comparison, we similarly generate and show distributions for a constant phase velocity model that has $\frac{d\theta}{dt} = \omega_0$. This model has a flat distribution of phases and can be considered purely sinusoidal. In this special case, the orientation angle distribution function consistent with equation 15 and equation 16 is

$$p(\phi)_{\text{sinusoidal}} = \frac{1}{\pi} \frac{1 + \tan^2(\phi - \phi_{\text{tilt}})}{\sqrt{\pi_A^2 - \tan^2(\phi - \phi_{\text{tilt}})}}. \quad (17)$$

The phase velocity distribution for the oscillator chain model shown in Figure 11b shows two peaks, a low one for when there are interactions between neighboring oscillators and a high one that is at the intrinsic phase velocity. This is what we would expect from inspection of the phase velocities in Figure 9. Figure 11c shows orientation angles ϕ computed with no tilt, $\phi_{\text{tilt}} = 0$, and ratio $\pi_A = A\omega_0/v = 1$. Orientation angle distributions for both oscillator chain model and constant phase velocity model exhibit two peaks and a trough. In Figure 11c, the constant phase velocity model distribution, in orange, is consistent with the distribution function of equation 17 that is shown with a dotted red line. The peaks of the orientation angle distribution for the oscillator chain model have different heights due to the uneven phase velocity distribution, whereas the distribution is symmetrical about $\phi = 0$ for the sinusoidal (constant phase velocity) model.

We can compare the modeled distribution of body orientations to those measured in our videos of the eels engaged in the metachronal wave, shown in Figure 7b, and discussed in section IV A. Figure 11d shows orientation angle distributions computed with $\phi_{\text{tilt}} = 20^\circ$ and ratio $\pi_A = 0.7$ which is that of equation 11. To facilitate comparison between distributions we have smoothed the model distributions using a Gaussian filter with standard deviation of 12° . In Figure 11c, we replot one of the orientation angle distributions that was shown in Figure 7b and is measured from Video B of a metachronal

wave. The model orientation distributions shows two peaks, and when corrected by the same factor (setting $\pi_A = \pi_{A,MW}$) and smoothed, they have a width and two peaks similar to that observed for the metachronal wave. Unlike the observed distribution, the sinusoidal model's orientation angle distribution is symmetrical about ϕ_{tilt} and its two peaks are the same height. In contrast, the oscillator chain model distribution is asymmetric or lopsided and its two peaks have different heights. Because there are variations in oscillator phase velocity in the oscillator chain model, the associated orientation angle distribution is lopsided. The oscillator chain model offers an explanation for the asymmetry that is present in the observed orientation angle distribution.

To compare the oscillator chain model to the observed orientation angle distribution we smoothed the model. Noise-like variations in the observed orientation angle distribution can be due to eels that are not aligned with their neighbors and variations in shading that affect the accuracy of the HOG algorithm. The oscillator chain model's distribution is more lopsided than the observed distribution which implies that variations in the phase velocity are not as extreme as predicted in Figure 11b. A more complex oscillator chain model would be needed to give a better fit to the observed orientation angle distribution.

E. Body shapes

In equation 15 we used model phases to compute the distribution of body orientation angles ϕ assuming a constant wave velocity v . With the same assumption we can compute the position and shape of the entire body using a time series of model outputs. Our procedure for doing this is described in appendix B.

In Figure 12a we show computed eel body shapes that are derived from the integrated phase oscillator model output shown in Figure 9 (integrating equation 10) and computed along the body lengths using equation B7. To generate the body positions we used amplitude $A = 0.07$ mm, (based on that measured from eel head motions for eels engaged in the metachronal wave), and intrinsic phase velocity $\omega_0 = 2\pi f_u$ with $f_u = 5.9$ Hz based on freely swimming eels. We adopted tilt angle $\phi_{\text{tilt}} = 20^\circ$ (the same as we used to generate orientation distributions in Figure 11). To match the metachronal wavelength we used a horizontal distance between eel mean centerlines of $D = 0.11$ mm, (as defined in Figure 8). Lastly we use a wave speed $v = 4.1$ mm/s. The ratio $\pi_A = A\omega_0/v = 0.63$ is similar to given in equation 11 and was used to create the model orientation distributions in Figure 11d. The eel body shapes using these parameters are shown in Figure 12a and they illustrate similar morphology to the vinegar eels themselves when engaged in the metachronal wave. Figure 12b shows a panel like those of Figure 3 from Video B for comparison.

Figure 12a shows that the periodic variations in phase

delay and phase velocity of an entrained state from our oscillator chain model (equation 10) reduce overlap between eels, not just near the eel heads but throughout their bodies. The eel bodies are nearly equidistant from each other everywhere. In Figure 12c we show body positions generated with a constant phase velocity (ω_0) and constant phase delay (with the same wavelength N_λ) model. The constant phase delay and phase velocity model fails badly. Variations in phase delay between neighboring eels and in their phase velocity during different parts of the oscillation are probably needed to prevent strong steric interactions between the eels.

We chose the wave speed v along the body to best match the observed morphology, however it exceeds both the metachronal wave speed of about $v_{MC} \sim 3.7$ mm/s and the undulation wave speed on the 1 mm long freely swimming eel of $v_u \sim 3.0$ mm/s. We might expect $v = v_{MC}/\cos \phi_{\text{tilt}} = 3.9$ mm/s using $v_{MC} = 3.7$ mm/s and $\phi_{\text{tilt}} = 20^\circ$. Our chosen value for v exceeds this. Our assumption for computing orientation angle ϕ in equation 15 and body shape ignores interactions between organisms that should affect the speed of wave propagation down the eel bodies. A more complex model that takes into account proprioception feedback throughout the eels body lengths might give a smoother and more symmetric orientation angle distribution, (reducing the discrepancy between that modeled and measured in Figure 11d) and a closer match to the wave morphology (improving the comparison between Figure 12a and b). We observe that the amplitude of motion in the metachronal wave $A_{MW} > A_u$ exceeds the amplitude of undulation when freely swimming, $A_{MW} > A_u$ and the speed of waves traveling down the body exceeds that when freely undulating $v > v_u$. A feedback motor control model, perhaps based on local body curvature, might predict or explain these characteristics.

There is a discrepancy between the overlap parameter $\beta = d/A = 0.25$ of the numerical oscillator model we adopted (shown in Figure 9 and used to create Figures 11 and 12) and that derived from the additional parameters we used to make Figure 12a for the eel bodies. The distance between eel centerlines d is related to the horizontal distance between mean centerlines D with $d = D \sin \phi_{\text{tilt}}$ (see Figure 8). For the model shown in Figure 12a, we used $D = 0.11$ mm, $A = 0.07$ mm and $\phi_{\text{tilt}} = 20^\circ$ giving $d = 0.038$ mm. We can estimate an overlap parameter for the tilted system $\beta \sim D \sin \phi_{\text{tilt}}/A = 0.54$ which exceeds our oscillator model overlap. This discrepancy might be reduced if we included the eel body width and the tilt angle ϕ_{tilt} in our overlap criterion function. A more complex model that takes into account feedback throughout the eels body lengths might also resolve this discrepancy.

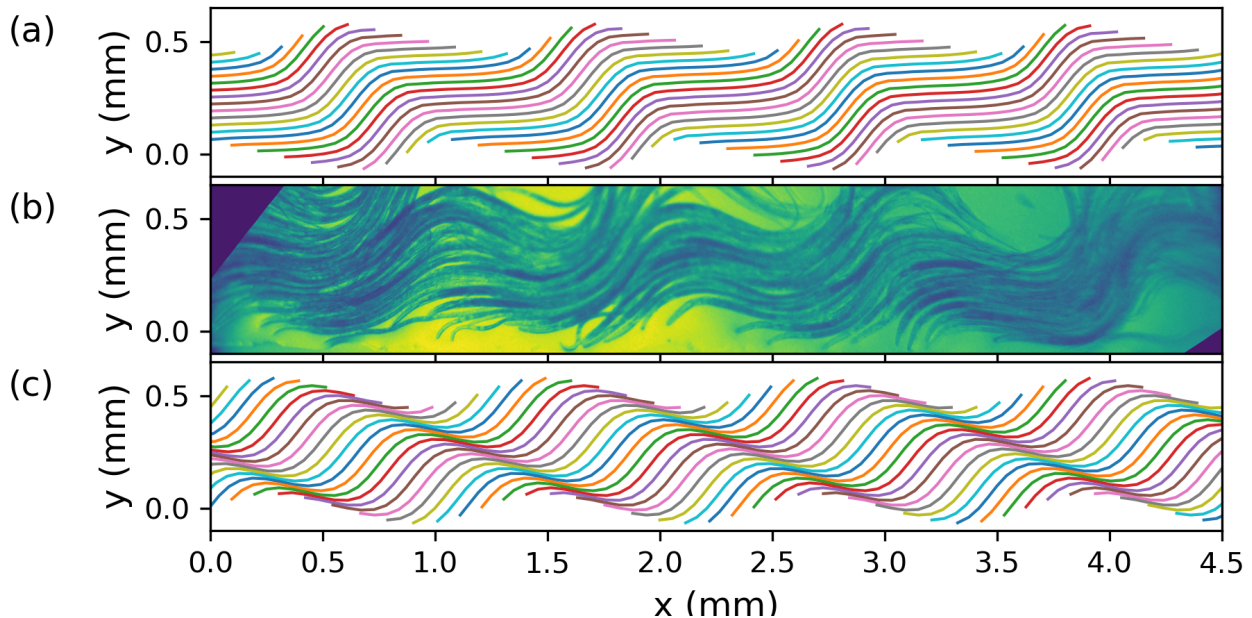


FIG. 12. (a) Eel body positions that are computed with a series of outputs at different times of the phase oscillator model shown in Figure 9 and using equation B7. Overlaps are reduced not only at the eel heads but throughout their body. (b) A panel from Video B similar to those shown in Figure 3. The morphology of the model wave in (a) resembles that seen in the vinegar eels. (c) Eel body positions were estimated via equation B7 but with a constant time delay and constant phase velocity model. Other parameters were the same. This model causes eel bodies to overlap. A comparison between (a) and (c) suggests that there must be variations in the phase velocities to reduce steric interactions.

VI. SUMMARY AND DISCUSSION

We presented high speed videos of swimming vinegar eel nematodes (*T. acetii*) at low and high concentration. In a drop containing a high concentration of the vinegar eels, the eels concentrate at the edge of a drop and engage in collective wave-like motion known as a metachronal wave. We found that freely swimming organisms have oscillation frequency of about 6 Hz. However, at high concentration the nematodes cluster on a boundary and exhibit traveling waves with a lower frequency of about 4 Hz. For a freely swimming vinegar eel, the body shape is nearly sinusoidal over much of its body length. In contrast, the distribution of body orientation angles for organisms engaged in the metachronal wave has two peaks of different heights, implying that the motion is not purely sinusoidal. The bodies spend more time at higher orientation angles w.r.t to their mean body orientation angle (averaged over a cycle).

We constructed a model for the collective behavior based on a chain of phase oscillators. Because we do not see large drifts in the mean eel head positions, averaged over an oscillation cycle, we neglect the head's forward motion. Because experiments of a similar nematode, *C. elegans*, support a model where the undulation is initiated at the head [37], we use the phase of the head's back and forth motion to describe it as an oscillator. Because the metachronal wave frequency is lower than the undulation frequency of a freely swimming eel,

we adopt interactions that reduce the oscillator phase velocity. Our oscillator model uses strong but directed or one-sided nearest neighbor to mimic steric interactions between organisms. The oscillator model (equation 10) robustly exhibits entrained or traveling wave solutions and can have traveling waves with wavelength (in terms of numbers of organisms or oscillators) and mean phase velocity (in units of the intrinsic or freely swimming undulation frequency) similar to that of the vinegar eels when engaged in a metachronal wave.

To estimate the distribution of body orientation angles and body shapes from our oscillator model, we assume that the undulation waves propagating down the body from the eel head have a constant wave velocity. This gives a two humped distribution of body orientations with peaks of different heights, similar to that observed for vinegar eels engaged in the metachronal wave. The body shapes are similar to those engaged in the wave and the eel bodies don't overlap over their entire length. The model which was designed to impede eel head overlaps also reduces close interactions throughout the eel bodies.

Our model neglects interactions between organisms that should affect the amplitude and speed of wave propagation down the eel bodies. Our model also neglects the ability of the eels to change direction and congregate. Improved models could take into account the positions and phases of all points in the eel's bodies and allow them to swim, reorient and congregate.

Few known simple phase oscillator models exhibit a

large basin of attraction to an entrained or traveling wave state. Perhaps our model (given in equation 10) and that by Niedermayer et al. [13] can serve as examples that might give insight for more general classification of coupled phase oscillator models that would be helpful for predicting wavelike collective behavior.

Vinegar eels are visible by eye and are large compared to other biological systems that exhibit metachronal waves, such as carpets of cilia [12, 15, 52] or flagella on the surface of *Volvox carteri* alga colonies [14]. Their large size facilitates study, however it also places them in an interesting intermediate hydrodynamic regime, with swimming Reynolds number $Re = v_{\text{swim}}L/\nu \sim 0.4$ (where $\nu \sim 1 \text{ mm}^2\text{s}^{-1}$ is the kinematic viscosity of water), so the nature of hydrodynamic interactions between them should differ from that of microorganisms which are at much lower Reynolds number (e.g., [16, 53]). Their proximity when involved in collective behavior suggests that steric interactions may be important. Studies of the similar nematode *C. elegans* locomotion [37] imply that feedback in motor control affects their gait. It is exciting to have a relatively large system in which collective motion can be studied, however, this system also presents new challenges for understanding its behavior.

In on-going studies we will describe experiments of concentrations of *C. elegans*, explore collectively formed dense coherent filaments in *T. aceti* that we have observed advance on a vinegar/oil interface and explore the role of concentration, drop shape and wetting angle in affecting metachronal wave formation in *T. aceti* [29]. Similarities between *T. aceti* and *C. elegans* suggest that it may be possible to use techniques developed for *C. el-*

egans to perform genetic modifications on the *T. aceti* nematode. In future, genetically modified strains may help us better understand the molecular underpinnings of the collective motion. Future studies could question whether there is an evolutionary advantage to the collective behavior which may help populations of nematodes penetrate crowded environments to reach food or drive flows that transport oxygen and nutrients.

ACKNOWLEDGMENTS

We thank Ed Freedman for the gift of a microscope. We thank Kanika Vats for advice with filming through a microscope and letting us try filming at high speed with an inverted microscope. We thank William Houlihan for lending us an inverted microscope. We thank Nick Reilly for obtaining a centrifuge and showing us how to use it. We thank Doug Portman for helpful discussions on *C. elegans*. We thank Keith Nehrke, Sanjib K. Guha, Yunki Im and other members of Nehrke's lab for helping us explore *C. elegans*, teaching us how to culture *C. elegans* and giving us some materials and live worms to culture in our lab. We thank Steve Teitel, Sanjib K. Guha, Keith Nehrke and Randal C. Nelson for helpful suggestions and discussions.

This material is based upon work supported in part by NASA grants 80NSSC21K0143 and 80NSSC17K0771, National Science Foundation Grant No. PHY-1757062, and National Science Foundation Grant No. DMR-1809318.

-
- [1] M. C. Marchetti, J. F. Joanny, S. Ramaswamy, T. B. Liverpool, J. Prost, M. Rao, and R. A. Simha, *Reviews of Modern Physics* **85**, 1143 (2013).
 - [2] B. L. Partridge, *Scientific American* **246**, 114 (1982), ISSN 00368733, 19467087, URL <http://www.jstor.org/stable/24966618>.
 - [3] D. S. Calovi, U. Lopez, S. Ngo, C. Sire, H. Chaté, and G. Theraulaz, *New Journal of Physics* **16**, 015026 (2014), URL <https://doi.org/10.1088%2F1367-2630%2F16%2F1%2F015026>.
 - [4] J. Buck and E. Buck, *Nature* **211**, 562 (1966), URL <https://doi.org/10.1038%2F211562a0>.
 - [5] S. Strogatz, *Sync: How Order Emerges From Chaos In the Universe, Nature, and Daily Life* (Hachette Books, 2012), ISBN 9781401304461, URL <https://books.google.com/books?id=vHw44RSi0CwC>.
 - [6] S. H. Strogatz, D. M. Abrams, A. McRobie, B. Eckhardt, and E. Ott, *Nature* **438**, 43 (2005), URL <https://doi.org/10.1038%2F438043a>.
 - [7] G. I. Taylor, *Proceedings of the Royal Society of London. Series A. Mathematical and Physical Sciences* **209**, 447 (1951), URL <https://doi.org/10.1098%2Frspa.1951.0218>.
 - [8] N. Uchida and R. Golestanian, *Phys. Rev. Lett.* **106**, 058104 (2011), URL <https://link.aps.org/doi/10.1103/PhysRevLett.106.058104>.
 - [9] K. P. O'Keeffe, H. Hong, and S. H. Strogatz, *Nature Communications* **8**, 1504 (2017), URL <https://doi.org/10.1038%2Fs41467-017-01190-3>.
 - [10] A. Winfree, *Science* **298**, 2336 (2002).
 - [11] P. Lenz and A. Ryskin, *Phys. Biol.* **8**, 285 (2006).
 - [12] S. L. Tamm, T. M. Sonneborn, and R. V. Dippell, *The Journal of Cell Biology* **64**, 98 (1975), URL <https://doi.org/10.1083%2Fjcb.64.1.98>.
 - [13] T. Niedermayer, B. Eckhardt, and P. Lenz, *Chaos: An Interdisciplinary Journal of Nonlinear Science* **18**, 037128 (2008), URL <https://doi.org/10.1063%2F1.2956984>.
 - [14] D. R. Brumley, M. Polin, T. J. Pedley, and R. E. Goldstein, *Physics Review Letters* **109**, 268102 (2012).
 - [15] J. Elgeti and G. Gompper, *PNAS; Proceedings of the National Academy of Sciences* **110**, 4470 (2013).
 - [16] J. Elgeti, R. G. Winkler, and G. Gompper, *Reports on Progress in Physics* **78**, 056601 (2015), URL <https://doi.org/10.1088%2F0034-4885%2F78%2F5%2F056601>.
 - [17] S. Gueron and K. Levit-Gurevich, *Biophysical Journal* **74**, 1658 (1998), URL <https://doi.org/10.1016%2Fs0006-3495%2898%2977879-8>.
 - [18] A. Vilfan and F. Jülicher, *Physical Review Letters*

- 96, 058102 (2006), URL <https://doi.org/10.1103/2Fphysrevlett.96.058102>.
- [19] C. B. Lindemann and K. A. Lesich, *Journal of Cell Science* **123**, 519 (2010), URL <https://doi.org/10.1242/2Fjcs.051326>.
- [20] N. Uchida and R. Golestanian, *The European Physical Journal E* **35** (2012), URL <https://doi.org/10.1140/2Fepje%2Fi2012-12135-5>.
- [21] R. Chelakkot, M. F. Hagan, and A. Gopinath, *Soft Matter* **x**, x (2021), URL <https://doi.org/10.1039/2Fd0sm01162b>.
- [22] G. Ermentrout and N. Kopell, *Comm. Pure Appl. Math.* **49**, 623 (1986).
- [23] G. Ermentrout and N. Kopell, *SIAM J. Appl. Math.* **50**, 1014 (1990).
- [24] L. Ren and B. Ermentrout, *Physica D: Nonlinear Phenomena* **143**, 56 (2000), URL <https://doi.org/10.1016/2Fs0167-2789%2800%2900096-8>.
- [25] P. Muruganandam, F. F. Ferreira, H. F. El-Nashar, and H. A. Cerdeira, *Pramana* **70**, 1143 (2008), URL <https://doi.org/10.1007/2Fs12043-008-0119-8>.
- [26] P. F. C. Tilles, F. F. Ferreira, and H. A. Cerdeira, *Physical Review E* **83**, 066206 (2011), URL <https://doi.org/10.1103/2Fphysreve.83.066206>.
- [27] K. Dénes, B. Sándor, and Z. Nédá, *Communications in Nonlinear Science and Numerical Simulation* **78**, 104868 (2019), ISSN 1007-5704, URL <http://www.sciencedirect.com/science/article/pii/S1007570419301881>.
- [28] A. Peshkov (2019), lab experiments Oct 2019.
- [29] A. Peshkov, S. McGaffigan, and A. C. Quillen, *Wiggling droplets: metachronal waves in populations of turbotriax aceti*, preprint <https://arxiv.org/abs/2104.10316> (2021).
- [30] T. Vicsek, A. Czirok, E. Ben-Jacob, I. Cohen, and O. Shochet, *Physical Review Letters* **75**, 1226 (1995).
- [31] J. Yuan, D. M. Raizen, and H. H. Bau, *J. R. Soc. Interface* **12**, 20150227 (2015).
- [32] J. Yuan, D. M. Raizen, and H. H. Bau, *PNAS* **111**, 6865 (2014).
- [33] T. Sugi, H. Ito, M. Nishimura, and K. H. Nagai, *Nature Communications* **10**, 683 (2019).
- [34] See Supplemental Material at [URL] for video A, a high speed 1057 frames per second video of vinegar eels (*T. aceti*) at low concentration seen under the microscope.
- [35] See Supplemental Material at [URL] for video B, a high speed 1057 frames per second video of vinegar eels (*T. aceti*) at high concentration seen under the microscope.
- [36] J. Sznitman, X. Shen, R. Sznitman, and P. E. Arratia, *Physics of Fluids* **22**, 121901 (2010).
- [37] Q. Wen, M. D. Po, E. Hulme, S. Chen, X. Liu, S. W. Kwok, M. Gershow, A. M. Leifer, V. Butler, C. Fang-Yen, et al., *Neuron* **76**, 750 (2012).
- [38] N. Dalal and B. Triggs, in *2005 IEEE Computer Society Conference on Computer Vision and Pattern Recognition (CVPR 05)* (IEEE, 2005), URL <https://doi.org/10.1109/2Fcvpr.2005.177>.
- [39] J. Gray and H. W. Lissmann, *J. Exp. Biol.* **41**, 135 (1964).
- [40] N. Cohen and T. Sanders, *Current Opinion in Neurobiology* **25**, 99 (2014).
- [41] G. Haspel and M. O'Donovan, *Journal of Neuroscience* **31**, 14611 (2011).
- [42] J. H. Boyle, S. Berri, and N. Cohen, *Frontiers in Computational Neuroscience* **6** (2012), URL <https://doi.org/10.3389/2Ffncom.2012.00010>.
- [43] E. Niebur and P. Erdős, *Biophysical Journal* **60**, 1132 (1991), ISSN 0006-3495, URL <http://www.sciencedirect.com/science/article/pii/S000634959182149X>.
- [44] F. Lebois, P. Sauvage, C. Py, O. Cardoso, B. Ladoux, P. Hersen, and J.-M. D. Meglio, *Biophysical Journal* **102**, 2791 (2012), ISSN 0006-3495, URL <http://www.sciencedirect.com/science/article/pii/S0006349512005516>.
- [45] S. Berri, J. H. Boyle, M. Tassieri, I. A. Hope, and N. Cohen, *HFSP Journal* **3**, 186 (2009), URL <https://doi.org/10.2976/2F1.3082260>.
- [46] J. A. Acebron, L. L. Bonilla, C. J. P. Vicente, F. Ritort, and R. Spigler, *Reviews of Modern Physics* **77**, 137 (2005).
- [47] Y. Kuramoto, in *Int. Symposium on Mathematical Problems in Theoretical Physics*, edited by H. Araki (Springer, 1975), vol. 39 of *Lecture Notes in Physics*, pp. 420–422.
- [48] Y. Kuramoto and I. Nishikawa, *Journal of Statistical Physics* **49**, 569 (1987), URL <https://doi.org/10.1007/2Fbf01009349>.
- [49] D. Aeyels and J. A. Rogge, *Progress of Theoretical Physics* **112**, 921 (2004).
- [50] Z. Zheng, G. Hu, and B. Hu, *Phys. Rev. Lett.* **81**, 5318 (1998).
- [51] B. Ottino-Löffler and S. H. Strogatz, *Physical Review E* **94**, 062203 (2016), URL <https://doi.org/10.1103/2Fphysreve.94.062203>.
- [52] S. L. Tamm and G. A. Horridge, *Proceedings of the Royal Society of London. Series B, Biological Sciences* **175**, 219 (1970), ISSN 00804649, URL <http://www.jstor.org/stable/76025>.
- [53] W. Gilpin, M. S. Bull, and M. Prakash, *Nature Reviews Physics* **2**, 74 (2020), URL <https://doi.org/10.1038/2Fs42254-019-0129-0>.

Appendix A: Compression and rarefaction in entrained states

The integration shown in Figure 9 of the model given by Equation 10 shows that each oscillator has a periodic trajectory but with two regions. One region has a low phase delay and phase velocity and the other region has a higher phase delay and phase velocity. We can also show this behavior by plotting phase angle θ against time for a series of oscillators. This type of plot is often used to study shock compression or rarefaction. On this plot, the inverse of the slope gives the phase velocity and the horizontal distance between consecutive lines gives the phase delay. We show such a plot in Figure 13 for an integration with the same parameters as in Figure 9. We plot phase θ vs time for 11 consecutive oscillators after integrating to $t = 1000$ and for a duration of $\Delta t = 10$. The region of lower phase velocity lies between the thick gray vertical lines which are at $\theta = 0.25\pi$ and 0.82π .

We make the assumption that an entrained state has two regions, like those seen at the end of the integrations shown in Figure 9 and in Figure 13. For our model in

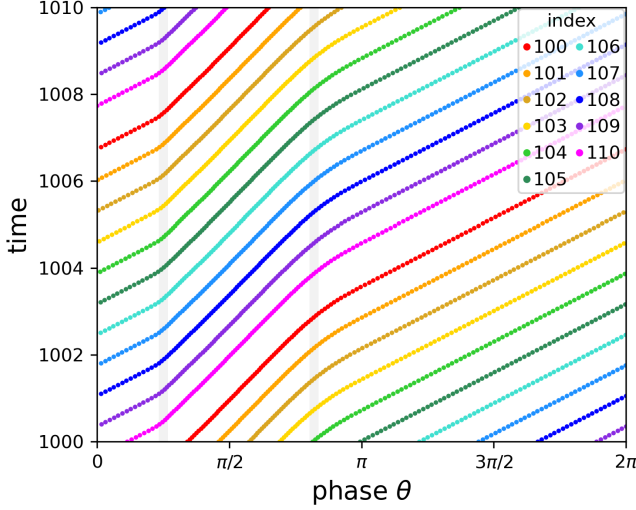


FIG. 13. We plot phase θ vs time for 11 consecutive oscillators for the directed chain oscillator model with the same parameters as shown in Figure 9. Each oscillator is plotted with a different color and the oscillator indices are given in the key. The figure shows the periodic compression and rarefaction of phase in the entrained state. The region of lower phase velocity, between $\theta \approx 0.25\pi$ and 0.82π , is marked with the vertical thick light gray lines. The inverse of the local slope of one of the curves gives the phase velocity and the horizontal distance between neighboring curves gives the phase delay between consecutive oscillators.

equation 10, which we repeat here for clarity,

$$\frac{d\theta_i}{dt}\omega_0^{-1} = 1 - \frac{K}{2} \left[\tanh \left(\frac{\cos \theta_{i-1} - \cos \theta_i - \beta}{h_{ol}} \right) + 1 \right]. \quad (\text{A1})$$

the high value of the phase velocity is the intrinsic phase velocity ω_0 and the low value is $\omega_0(1-K)$. An entrained state has a phase delay τ where

$$\theta_j(t + \tau) = \theta_{j+1}(t). \quad (\text{A2})$$

We expand the left side to first order in τ and write θ_{j+1} in terms of the phase delay $\chi_j = \theta_{j+1} - \theta_j$, giving

$$\dot{\theta}_j(t)\tau \approx \chi_j. \quad (\text{A3})$$

We denote the phase delay for the slower state as χ_s and that of the faster state as χ_f . Equation A3 gives

$$\begin{aligned} \chi_s &\approx \omega_0(1-K)\tau \\ \chi_f &\approx \omega_0\tau. \end{aligned} \quad (\text{A4})$$

In the fast and slow regions, the phase velocity is constant and phase differences between oscillators are maintained. The properties of the entrained states must be set by the transition regions. We consider two oscillators, one in the slow region and the other that is exiting the slow region. We can estimate the change in phase delay

between the two regions from the time Δt_{fs} it takes a single oscillator to exit the slow region

$$\chi_f - \chi_s \approx \Delta t_{fs} \tilde{\omega}, \quad (\text{A5})$$

where

$$\tilde{\omega} \approx (1 - K/2)\omega_0 \quad (\text{A6})$$

is the average phase velocity. We use equation A5 to estimate the phase delay τ .

For small phase delay $\chi_{j-1} = \theta_j - \theta_{j-1}$ equation A1 can be written to first order in phase shift χ_{j-1} as

$$\frac{d\theta_j}{dt}\omega_0^{-1} \approx 1 - \frac{K}{2} \left[\tanh \left(\frac{\sin \theta_j \chi_{j-1} - \beta}{h_{ol}} \right) + 1 \right]. \quad (\text{A7})$$

The time Δt_{fs} it takes oscillator j to pass through the transition from slow to fast regions we estimate from the time it takes $|\sin \theta_j \chi_{j-1}|/h_{ol}$ to change by about 2 (corresponding the region of high slope for the tanh function). This transition time is approximately

$$\Delta t_{fs} \sim 2h_{ol} \left| \cos \theta_j \frac{d\theta_j}{dt} \chi_{j-1} \right|^{-1}. \quad (\text{A8})$$

We assume that the transition boundaries are where $|\cos \theta| \sim 1$ and take an average of the fast and slow values for $\frac{d\theta}{dt}$ and χ (using equations A4 and A6) to estimate the duration of the transition from a fast to slow region or vice versa

$$\Delta t_{fs} \sim \frac{8h_{ol}}{(\chi_f + \chi_s)(2-K)\omega_0}. \quad (\text{A9})$$

Using equations A5 and A4 we estimate the delay τ

$$\tau \sim \frac{2}{\omega_0} \sqrt{\frac{h_{ol}}{K(2-K)}} \quad (\text{A10})$$

and the wavelength

$$N_\lambda \sim \frac{2\pi}{\tilde{\omega}\tau} \sim 2\pi \sqrt{\frac{K}{(2-K)h_{ol}}}. \quad (\text{A11})$$

For $h_{ol} = 0.05$ and $K = 0.5$ this gives $N_\lambda \sim 16$ which is a reasonable value but exceeds the value of 12 we see in the integration shown in Figure 13. We verified that N_λ decreases with increasing h_{ol} , though it does not decrease as quickly as predicted by equation A11. A better prediction would take into account the phases of the transitions and the difference between compression and rarefaction transitions. The comparison between estimated and numerically measured wavelengths suggests that techniques used to study non-linear differential equations may be useful for predicting the properties of entrained states.

Appendix B: Predicting body positions and shapes from a phase oscillator model

In this section we show how we compute eel body shapes and positions from an oscillator chain model. We assume the eel head positions are described by a chain of oscillators as illustrated in Figure 8. We assume that waves propagate down the body with a constant speed v .

We adopt an Cartesian coordinate system $\mathbf{X} = (X, Y)$ on the plane to describe positions of points on the body of a chain of eels, as shown in Figure 8b. We assume the mean centerline position of the i -th eel's head has coordinates $\mathbf{X}_{i,hc}$ and the eel's mean centerline is tilted by angle ϕ_{tilt} with respect to the horizontal direction. We assume that the mean centerline head positions are fixed and are equally spaced on the X axis

$$\mathbf{X}_{i,hc} = \begin{pmatrix} iD \\ 0 \end{pmatrix}, \quad (\text{B1})$$

where D is the horizontal distance between the mean centerlines. We assume the wave travels down the body with velocity v , as given in equation 13 which we repeat here

$$y_i(x, t) = A \cos \left[\theta_i \left(t - \frac{x}{v} \right) \right]. \quad (\text{B2})$$

The i -th eel's head position is at $y(x = 0, t)$. Here x is the distance along the mean centerline and y_i is the distance perpendicular to it. We rotate the centerlines by ϕ_{tilt} so that in the (X, Y) coordinate system the head of the i -th eel is at

$$\mathbf{X}_{i,h}(t) = \begin{pmatrix} \cos \phi_{\text{tilt}} & -\sin \phi_{\text{tilt}} \\ \sin \phi_{\text{tilt}} & \cos \phi_{\text{tilt}} \end{pmatrix} \begin{pmatrix} 0 \\ A \cos(\theta_i(t)) \end{pmatrix} + \mathbf{X}_{i,hc}. \quad (\text{B3})$$

We can use the coordinate along the mean centerline x

to specify body positions

$$\mathbf{X}_i(x, t) = \begin{pmatrix} \cos \phi_{\text{tilt}} & -\sin \phi_{\text{tilt}} \\ \sin \phi_{\text{tilt}} & \cos \phi_{\text{tilt}} \end{pmatrix} \begin{pmatrix} x \\ A \cos \left[\theta_i \left(t - \frac{x}{v} \right) \right] \end{pmatrix} + \mathbf{X}_{i,hc}. \quad (\text{B4})$$

With $x = 0$, this is consistent with equation B3 for the i -th eel's head.

Using equation B2, at $t = 0$, the y position of the i -th eel is determined by its head position at an earlier time,

$$y_i(x, t = 0) = A \cos \left[\theta_i \left(-\frac{x}{v} \right) \right], \quad (\text{B5})$$

where the earlier time is

$$t' = -\frac{x}{v}. \quad (\text{B6})$$

Using a phase oscillator model we can generate arrays of phases θ_i at a series of times. The arrays at different output times t' then can be used to predict the \mathbf{X} positions at $t = 0$ along the eel's bodies;

$$\mathbf{X}_i(t') = \begin{pmatrix} \cos \phi_{\text{tilt}} & -\sin \phi_{\text{tilt}} \\ \sin \phi_{\text{tilt}} & \cos \phi_{\text{tilt}} \end{pmatrix} \begin{pmatrix} -vt' \\ A \cos [\theta_i(t')] \end{pmatrix} + \begin{pmatrix} iD \\ 0 \end{pmatrix}, \quad (\text{B7})$$

where we have used equations B1, B4 and B6.

From a series of phase arrays computed at different output times for the phase oscillator model of equation 10 we can generate eel body positions using equation B7. To do this we require values for the velocity of waves along the eel body v , the amplitude A , the horizontal distance between the mean positions of organism heads D and the body tilt angle ϕ_{tilt} . Also, the outputs of the integration must be put in units of time using the intrinsic oscillator phase velocity ω_0 .